J. Fluid Mech. (2025), *vol.* 1018, A2, doi:10.1017/jfm.2025.10496

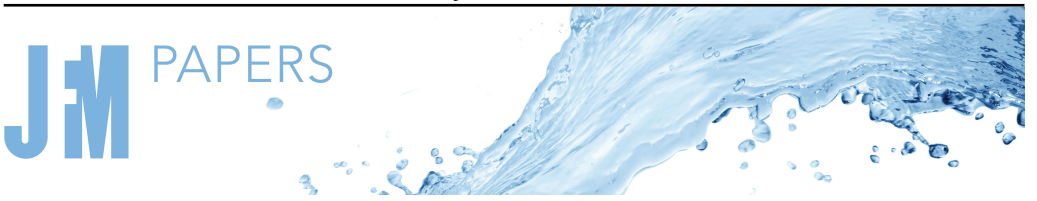

Analysis of large-scale spanwise motions in shock wave–turbulent boundary-layer interactions

Zhen Zhang[1], **Xin Li**[1] and **Jiaao Hao**[1]

[1]Department of Aeronautical and Aviation Engineering, The Hong Kong Polytechnic University, Kowloon, Hong Kong, PR China

Corresponding author: Jiaao Hao, jiaao.hao@polyu.edu.hk

(Received 13 January 2025; revised 31 May 2025; accepted 18 July 2025)

Large-scale spanwise motions in shock wave–turbulent boundary-layer interactions over a 25° compression ramp at Mach 2.95 are investigated using large-eddy simulations. Spectral proper orthogonal decomposition (SPOD) identifies coherent structures characterised by low-frequency features and a large-scale spanwise wavelength of $O(15\delta_0)$, where δ_0 is the incoming boundary-layer thickness. The dominant frequency is at least one order of magnitude lower than that of the shock motions. These large-scale spanwise structures are excited near the shock foot and are sustained along the separation shock. Global stability analysis (GSA) is then employed to investigate the potential mechanisms driving these structures. The GSA identifies a stationary three-dimensional (3-D) mode at a wavelength of $15\delta_0$ with a similar perturbation field, particularly near the separation shock. Good agreement is achieved between the leading SPOD mode and the 3-D GSA mode both qualitatively and quantitatively, which indicates that global instability is primarily responsible for the large-scale spanwise structures surrounding the shock. The reconstructed turbulent separation bubble (TSB) using the 3-D global mode manifests as spanwise undulations, which directly induce the spanwise rippling of the separation shock. Furthermore, the coupled TSB motions in the streamwise and spanwise directions are examined. The TSB oscillates in the streamwise direction while simultaneously exhibiting spanwise undulations. The filtered wall-pressure signals indicate the dominant role of the streamwise motions.

Key words: turbulent boundary layers, shock waves, boundary layer separation

1. Introduction

Shock wave–turbulent boundary-layer interactions (STBLIs) occur in a broad range of high-speed devices, including supersonic intakes, over-expanded rocket nozzles and transonic airfoils. The presence of low-frequency unsteadiness and large-scale flow structures in STBLIs has been extensively reported in previous studies (Dussauge, Dupont & Debiève 2006; Clemens & Narayanaswamy 2014).

Significant efforts have been devoted to exploring the physical origin of low-frequency unsteadiness in STBLIs. Two main mechanisms have been proposed to explain the unsteadiness: upstream and downstream mechanisms (Souverein *et al.* 2010; Clemens & Narayanaswamy 2014). The upstream mechanism suggests that the shock motions are influenced by the upstream turbulent boundary layer (TBL). Beresh, Clemens & Dolling (2002) identified a relationship between the upstream TBL and the shock motions: a fuller velocity profile causes the shock to move downstream (and *vice versa*). This relationship was verified by Hou, Clemens & Dolling (2003) using particle image velocimetry (PIV) experimentally. Later, Ganapathisubramani *et al.* (2007, 2009) discovered superstructures in the upstream TBL with streamwise lengths of $(40-50)\delta_0$ using PIV and Taylor's hypothesis, where δ_0 is the boundary-layer thickness. These superstructures were believed to be vital in driving the low-frequency unsteadiness. Regarding the downstream mechanism, much attention has been paid to connecting the dynamics of the separation bubble with the unsteady separation shock movement. Pirozzoli & Grasso (2006) performed a short-time direct numerical simulation in a Mach 2.25 impinging shock interaction. They modelled the low-frequency unsteadiness as acoustic resonance similar to Rossiter modes (Rossiter 1964) in cavity flows. Piponniau *et al.* (2009) investigated the relation between the shock position and the turbulent separation bubble (TSB) size based on conditionally averaged PIV velocity fields of an impinging shock interaction. They found that the shock moves upstream when the TSB size is large and downstream when the TSB size is small. They proposed a self-sustained model in which mass loss due to fluid entrainment is recharged by the flapping of the TSB. Subsequently, Touber & Sandham (2011) developed a mathematical model to illustrate the low-frequency motions, similar to the Plotkin model (Plotkin 1975). They argued that the low-frequency unsteadiness is an intrinsic property but needs to be excited by extrinsic low-frequency disturbances. Grilli *et al.* (2012) and Pasquariello, Hickel & Adams (2017) also numerically verified the intrinsic mode in a compression ramp and impinging shock interaction, respectively. Recently, Hao (2023) drew a similar conclusion based on Reynolds-averaged Navier–Stokes (RANS) equations and linear stability analysis. Clemens & Narayanaswamy (2014) summarised that both upstream and downstream mechanisms may work in shock-induced turbulent separated flows, whereas the dominant mechanism may depend on the interaction strengths.

Although much work has been done to understand the nominally two-dimensional (2-D) dynamics of STBLIs, three-dimensional (3-D) effects associated with TSBs have received less attention, particularly concerning large-scale spanwise structures. These spanwise structures may lead to streaks of low and high heat flux distributions. Two types of large-scale spanwise structures have been reported: Görtler-like vortices downstream of the interaction region and large-scale spanwise motions within the interaction region. Generally, the scale of Görtler-like vortices is comparable to the boundary-layer thickness, while the latter's size is comparable to that of the separation region.

Streamwise vortices downstream of the interaction region have been widely reported in turbulent flows by numerical simulations (Loginov, Adams & Zheltovodov 2006; Priebe *et al.* 2016; Pasquariello *et al.* 2017) and experiments (Schuelein & Trofimov 2011; Li *et al.* 2022). These streamwise vortices, often referred to as Görtler-like vortices,

exhibit wavelengths of approximately $2\delta_0$ and are primarily caused by centrifugal effects. Floryan (1991) suggested that the Görtler-like vortices are influenced by disturbances in the upstream TBL and classified them as either steady or unsteady. The steady pattern means these vortices are visible in the time-averaged flow, typically represented by the contour of the mean skin-friction coefficient. For turbulent separated flows, both steady (Loginov *et al.* 2006; Grilli, Hickel & Adams 2013; Tong *et al.* 2017; Helm & Martín 2021) and unsteady (Priebe *et al.* 2016; Pasquariello *et al.* 2017; Li *et al.* 2022) patterns have been reported. However, there is no comprehensive research to elucidate the essential reasons for these different patterns, to the best of the authors' knowledge.

For the large-scale spanwise structures within the interaction region, Jenquin, Johnson & Narayanaswamy (2023) observed large-scale spanwise pressure undulations within the intermittent region at Mach 2.5 using 2-D surface pressure field imaging. They found that the shear layer events induced the upstream-propagating pressure perturbations in the vicinity of the reattachment region, which influenced the streamwise motions of the separation shock. However, the authors clearly noted that the sources of spanwise rippling in the separation shock could not be identified due to limitations in the signal-to-noise ratio. Ceci *et al.* (2023, 2024) conducted a series of non-swept and swept impinging shock interactions in wide computational domains. Their results revealed that spanwise structures near the mean separation line are proportional to the separation bubble size L_{sep}, with a characteristic spanwise wavelength of $\lambda_z \approx 2L_{sep}$. They proposed that these spanwise structures were responsible for the rippling of the separation line, behaving as large-scale spanwise corrugations. For non-swept STBLIs, they regarded these structures as the signatures of 2-D breathing motions. Liu *et al.* (2024) investigated multiscale spanwise unsteadiness in a sidewall-confined 25° compression ramp interaction. Their modal analysis revealed that low-frequency unsteadiness in the intermittent region consists of quasi-2-D streamwise oscillations and spanwise unsteadiness. While the streamwise oscillations correspond to the 2-D shock motions, the origins of the large-scale spanwise unsteadiness remained unknown. Similar large-scale structures associated with TSBs have also been reported in incompressible flows by Dau *et al.* (2023) and Borgmann *et al.* (2024). They observed spanwise structures with a wavelength of $0.8L_{sep}$ using spectral proper orthogonal decomposition (SPOD) of PIV data. Despite the differences in flow conditions and reported spanwise wavelengths, these studies consistently indicate the potential existence of large-scale spanwise structures associated with TSBs. These structures may provide a basis for understanding and modelling the 3-D motions of TSBs in nominally 2-D STBLIs.

Regarding the origins of the two types of large-scale spanwise structures: (i) Görtler-like vortices, which primarily arise from streamline concave curvature effects induced by TSBs; (ii) the recently reported structures within the intermittent region, whose physical explanation remains an open question. As suggested by Liu *et al.* (2024), stability analysis methods may provide valuable insights to the origins of the latter spanwise structures. Stability analysis methods, including resolvent analysis (McKeon & Sharma 2010) and global stability analysis (GSA), have recently gained popularity for uncovering linear mechanisms in turbulent flows. Resolvent analysis has been widely used to investigate dominant coherent structures in turbulent jets and channel flows (McKeon & Sharma 2010; Luhar, Sharma & McKeon 2014; Schmidt *et al.* 2018; Abreu *et al.* 2020), while two recent studies by Hao (2023) and Cura *et al.* (2024) effectively applied it to model low-frequency bubble dynamics. Global stability analysis has also been successfully utilised to analyse low-frequency shock motions in STBLIs (Touber & Sandham 2009; Pirozzoli *et al.* 2010; Nichols *et al.* 2017; Hao 2023). Notably, a comparison of the resolvent analysis and GSA

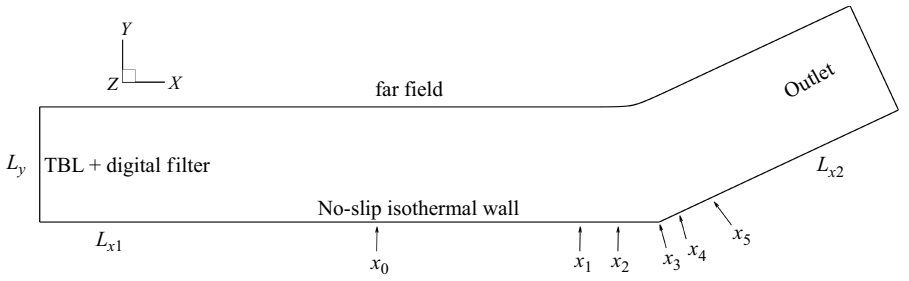

Figure 1. Computational domain and boundary conditions.

results reveals a modal resonance mechanism that drives low-frequency bubble breathing in both supersonic and low-speed flows (Hao 2023; Cura *et al.* 2024).

The objective of this study is to identify the mechanisms driving large-scale spanwise motions and to characterise the role of these motions in the dynamics of STBLIs. Specifically, this work focuses on three main aims: (i) validate the existence of these large-scale spanwise structures using modal analysis based on the large-eddy simulation (LES) database, as discussed in § 3.2; (ii) examine the origins of these structures through stability analysis, as detailed in § 4.1; (iii) analyse the 3-D motions of the TSB using pressure fluctuations in the interaction region, as discussed in § 4.2.

2. Computational set-up and numerical approach

2.1. *Computational set-up*

Figure 1 depicts the compression ramp configuration with a ramp angle of 25°. Throughout the paper, x, y and z denote the Cartesian coordinates, with the origin located at the corner. The domain sizes are as follows: $L_{x1} = 39.6\delta_0$, $L_{x2} = 17.6\delta_0$, $L_y = 7.3\delta_0$ and $L_z = 15\delta_0$, where $\delta_0 = 2.27$ mm is the TBL thickness at the reference position x_0. Stations $x_0 - x_5$ are located at $x = -17.5\delta_0$, $-4.9\delta_0$, $-2\delta_0$, 0, δ_0 and $3.5\delta_0$, respectively. The computational mesh consists of $1321 \times 136 \times 682$ grid points in the streamwise, wall-normal and spanwise directions. The mesh resolution is $\Delta x^+ \approx 20$, $\Delta z^+ \approx 10$, and $\Delta y_w^+ \approx 1.1$ (at the reference station x_0), which meets the grid requirement of LES (Choi & Moin 2012).

The free-stream parameters match those of the experiment conducted by Zheltovodov *et al.* (1990), with density $\rho_\infty = 0.314\ \mathrm{kg\,m^{-3}}$, temperature $T_\infty = 108$ K, Mach number $M_\infty = 2.95$ and Reynolds number $Re_{\delta_0} = 63500$. Implicit LES are performed using an in-house multi-block parallel finite-volume solver named PHAROS (Hao, Wen & Wang 2019; Hao & Wen 2020; Hao *et al.* 2021). The inviscid fluxes are solved by means of the low-dissipative sixth-order kinetic preserving scheme (Pirozzoli 2010) and the Ausm$^+$-up scheme (Liou 2006) with the fifth-order weighted essentially non-oscillatory reconstruction (Jiang & Shu 1996), using a switch based on the Jameson sensor (Jameson, Schmidt & Turkel 1981). The viscous terms are computed using the second-order central scheme. The third-order low-storage Runge–Kutta scheme is applied for time integration with a time step of 8 ns. The total simulation time is approximately 12.7 ms. Flow samples are collected for a duration of 11.2 ms ($3024\delta_0/u_\infty$) once the separation zone is fully established, which occurs after approximately 1.5 ms. Here, u_∞ represents the free-stream velocity. A perfect gas assumption is applied, with a Prandtl number of 0.72, a specific heat ratio of 1.4 and a turbulent Prandtl number of 0.9. The molecular viscosity μ is obtained from Sutherland's law.

Boundary conditions are also listed in the figure. The extended digital filter technique (Touber & Sandham 2009; Ceci *et al.* 2022) is employed to introduce inflow turbulence. A supersonic outflow boundary condition is applied to the outlet boundary. A sponge zone approximately $2\delta_0$ thick is placed at the far-field boundary to eliminate any reflections (Mani 2012). An isothermal no-slip boundary condition is implemented at the wall, with a fixed wall temperature $T_w = 275.4$ K, consistent with Loginov *et al.* (2006). Periodic boundary conditions are used in the spanwise directions.

2.2. *Global stability analysis*

Global stability analysis is based on the assumption of a triple decomposition of unsteady flow into three parts: mean flow, coherent structures and turbulent (or incoherent) fluctuations (Reynolds & Hussain 1972), given as

$$\boldsymbol{Q}(x, y, z, t) = \boldsymbol{Q_{2-D}}(x, y) + \boldsymbol{Q'}(x, y, z, t) + \boldsymbol{Q'^{,t}}(x, y, z, t), \tag{2.1}$$

where $\boldsymbol{Q}$ is the vector of conservative variables, $\boldsymbol{Q_{2-D}}$ is the 2-D Favre-averaged base flow, $\boldsymbol{Q'}$ is the 3-D perturbation (coherent) and $\boldsymbol{Q'^{,t}}$ is the vector of turbulent fluctuations (incoherent). Substituting (2.1) into the Navier–Stokes (N-S) equations and neglecting higher-order terms leads to

$$\frac{\partial \boldsymbol{Q'}}{\partial t} = \boldsymbol{\mathcal{A}}(\boldsymbol{Q_{2-D}})\,\boldsymbol{Q'}, \tag{2.2}$$

where $\boldsymbol{\mathcal{A}}$ is the linearised N-S operator. The terms involving the incoherent term $\boldsymbol{Q'^{,t}}$ in the operator $\boldsymbol{\mathcal{A}}$ are modelled by the eddy viscosity μ_t. This modelling approach, however, is valid when a sufficient scale separation exists between coherent structures and turbulent fluctuations, as demonstrated by Reynolds & Hussain (1972) and Reau & Tumin (2002). The perturbation $\boldsymbol{Q'}$ is written in the following modal form:

$$\boldsymbol{Q'}(x, y, z, t) = \hat{\boldsymbol{Q}}(x, y)\exp[i\beta z - i(\omega_r + i\omega_i)t], \tag{2.3}$$

where $\hat{\boldsymbol{Q}}$ is the 2-D eigenfunction, β is the spanwise wavenumber, ω_r is the angular frequency and ω_i is the growth rate. The flow is globally stable for $\omega_i < 0$ and unstable for $\omega_i > 0$. Substituting (2.3) into (2.2) leads to an eigenvalue problem, which is solved using the implicitly restarted Arnoldi method implemented in ARPACK (Sorensen *et al.* 1996) at a given wavenumber β. The key point in solving the problem is constructing and discretising the operator $\boldsymbol{\mathcal{A}}$, which consists of inviscid and viscous Jacobians. To improve the accuracy, the inviscid fluxes are computed using the modified Steger–Warming scheme near discontinuities and a central scheme in smooth regions, as detected by a modified Ducros sensor (Hendrickson, Kartha & Candler 2018). The viscous fluxes are obtained using a second-order central difference scheme. Boundary conditions are consistent with those in figure 1, except for the left boundary, which is set as the far field. Influences of grid resolution and domain size in GSA are verified in Appendix A.

Based on the Boussinesq approximation, μ_t can be calculated using a least-squares method (Lilly 1992), which has been widely applied in turbulent flows (Raiesi, Piomelli & Pollard 2011; Abe *et al.* 2012; Coleman, Rumsey & Spalart 2018; Fan *et al.* 2024). Furthermore, the frozen eddy-viscosity strategy (Carini *et al.* 2017) is employed. The GSA solver for laminar flows (Hao *et al.* 2021) is used, adopting the effective viscosity $\mu_{eff} = \mu_t + \mu$.

	$\delta_0\,(\mathrm{mm})^{-1}$	$\delta^*\,(\mathrm{mm})^{-1}$	$\theta\,(\mathrm{mm})^{-1}$	$C_f \times 10^3$
Zheltovodov *et al.* (1990)	2.27	0.795	0.150	1.79
Loginov *et al.* (2006)	2.27	0.840	0.161	2.05
Present LES	2.27	0.783	0.161	2.05

Table 1. Summary of mean-flow parameters for the TBL at the reference position x_0. δ_0, the nominal thickness of the TBL, based on $0.99u_\infty$; δ^*, the displacement thickness of the TBL; θ, the momentum thickness of the TBL; C_f, the skin-friction coefficient.

2.3. *Spectral proper orthogonal decomposition*

Spectral proper orthogonal decomposition (Lumley 2007) is utilised to identify coherent structures of turbulent flows. Similar to "standard" POD (Lumley 2007), SPOD aims to find an optimal orthogonal basis for flow data. However, SPOD modes evolve both in time and space. According to Towne, Schmidt & Colonius (2018), SPOD modes combine the features of both POD and dynamic mode decomposition, allowing for the identification of optimal coherent structures.

In this study, we follow the procedures outlined by Towne *et al.* (2018) and utilise their code to seek SPOD modes. First, the discrete Fourier transform is applied to the LES database, combining Welch's method (Welch 1967) and a standard Hamming window to minimise spectral leakage. This step transforms the flow data in time space into frequency space $\hat{(\cdot)}$. Then, the cross-spectral density tensor $\boldsymbol{S}$ can be constructed at each frequency, given as

$$\boldsymbol{S} = \hat{\boldsymbol{U}}\hat{\boldsymbol{U}}^*, \tag{2.4}$$

where $\hat{\boldsymbol{U}}$ is a data matrix containing flow data at the same frequency, and $(\cdot)^*$ is the Hermitian transpose. The next step is to solve an eigenvalue problem to obtain the eigenvalues $\boldsymbol{\Lambda}$ and the corresponding SPOD modes $\hat{\boldsymbol{\Psi}}$ at each frequency, given as

$$\boldsymbol{S}\boldsymbol{W}\hat{\boldsymbol{\Psi}} = \hat{\boldsymbol{\Psi}}\boldsymbol{\Lambda}, \tag{2.5}$$

where $\boldsymbol{W}$ is the weight matrix. For compressible flows, the compressible energy form defined by Chu (1965) is applied to $\boldsymbol{W}$. The SPOD modes are sorted by decreasing energy, i.e. $\lambda_{fk}^1 \geqq \lambda_{fk}^2 \geqq \ldots \geqq \lambda_{fk}^{n_{blk}}$. The subscript fk represents the kth frequency, while the superscript n_{blk} indicates the mode number. The first SPOD mode is referred to as the optimal mode because it is optimal in terms of energy. The second and subsequent modes are referred to as suboptimal modes.

3. Large-eddy simulation results

3.1. *Instantaneous and mean flow features*

Table 1 presents key properties of the TBL at the reference station x_0. Our results align well with previous experimental data (Zheltovodov *et al.* 1990) and LES results (Loginov *et al.* 2006). Figure 2(a) shows the Van Driest transformed mean velocity profile (Van Driest 1951) at x_0, where

$$y^+ = \frac{\bar{\rho}_w u_\tau y}{\bar{\mu}_w}, \quad U_{VD}^+ = \frac{1}{u_\tau}\int_0^{\bar{u}} \sqrt{\frac{\bar{\rho}}{\bar{\rho}_w}}\,\mathrm{d}\bar{u}. \tag{3.1}$$

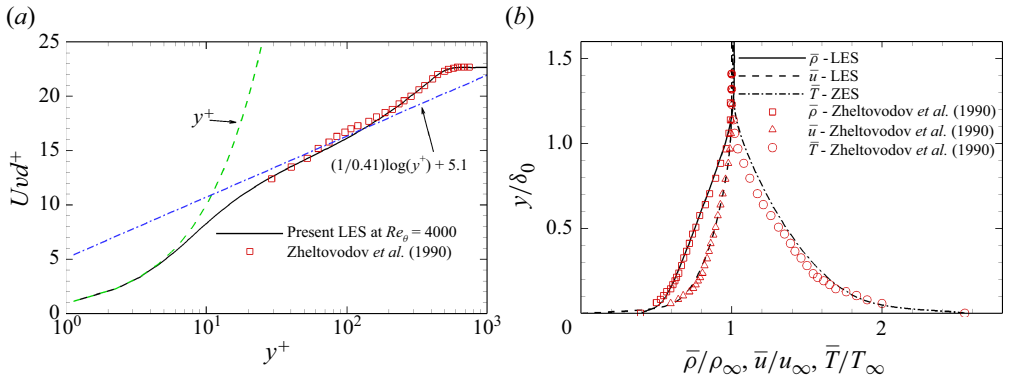

Figure 2. (*a*) Van Driest transformed mean velocity profile and (*b*) distributions of mean qualities of the TBL at the reference station x_0.

In these expressions, $\bar{\rho}_w$ is the mean wall density, $\bar{\mu}_w$ is the mean wall viscosity, u_τ is the friction velocity and $\bar{\rho}$ and $\bar{u}$ represent the mean density and streamwise velocity, respectively. Good agreement is achieved between the transformed velocity profile with the classical solutions $U_{VD}^+ = y^+$ and $U_{VD}^+ = (1/0.41)\ln y^+ + 5.1$, as well as with the experimental data (Zheltovodov *et al.* 1990). Figure 2(*b*) presents a comparison of the distributions of mean density $\bar{\rho}$, velocity $\bar{u}$ and temperature $\bar{T}$ with the experimental results, normalised by the free-stream parameters ρ_∞, u_∞ and T_∞. The computed density and velocity profiles show good agreement with the experimental data, while minor discrepancies are noted in the temperature profile.

The density-scaled root-mean-square (r.m.s.) intensities $\sqrt{\bar{\rho}/\bar{\rho}_w}(\cdot)'_{rms}/u_\tau$ (where $(\cdot)$ denotes streamwise velocity u, vertical velocity v and spanwise velocity w) of our results are compared with direct numerical simulations (DNS) results of incompressible and compressible TBLs (Wu & Moin 2009; Bernardini & Pirozzoli 2011) in figure 3. In the inner layer, the density-scaled r.m.s. values fall within two DNS databases. In the outer layer, the decreasing trends are also similar, with the velocity fluctuations approaching zero at $y = 1.4\delta_0$.

Figure 4 compares the distributions of the skin-friction coefficient C_f and the pressure coefficient C_p of our results with the experimental and LES results (Loginov *et al.* 2006). The values of C_f and C_p are defined by

$$C_f = \frac{2\tau_w}{\rho_\infty u_\infty^2}, \; C_p = \frac{2\bar{p}_w}{\rho_\infty u_\infty^2}, \tag{3.2}$$

where τ_w and $\bar{p}_w$ are the averaged wall shear stress and wall pressure, respectively. On the flat plate, the two LES results for C_f are nearly identical but slightly higher than the experimental data. Near the separation point, the skin friction decreases suddenly to negative values and recovers after reattachment. The separation and reattachment points of the previous LES results (Loginov *et al.* 2006) are located further downstream, while the separation lengths L_{sep} are both $7\delta_0$. As noted by Loginov *et al.* (2006), the minor discrepancy between the LES and experimental results in C_f distributions is influenced by two main factors: (i) experimental uncertainty (6 %−10 %) in skin-friction measurements (Borisov *et al.* 1993, 1999), and (ii) localised discrepancies stemming from the unspecified spatial alignment of experimental data relative to convergence–divergence-line pairs. Furthermore, 3-D flow relieving effects in experiments tend to decrease the separation length. Regarding C_p, all three distributions exhibit similar increases near the separation

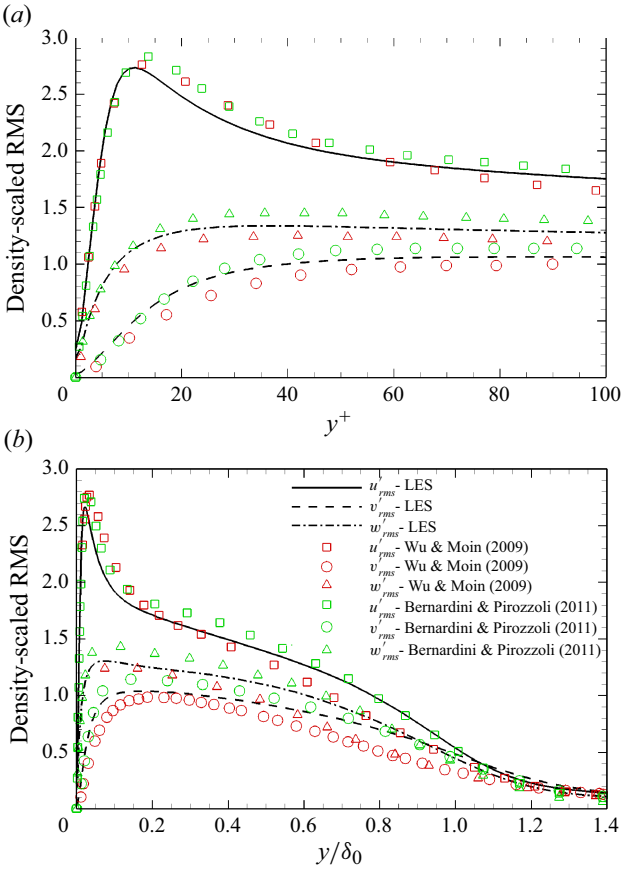

Figure 3. Density-scaled r.m.s. $\sqrt{\bar{\rho}/\bar{\rho}_w}(\cdot)'_{rms}/u_\tau$ (where $(\cdot)$ denotes streamwise velocity u, vertical velocity v and spanwise velocity w) at the reference station x_0 in inner layer (a) and outer layer (b). Wu & Moin (2009), incompressible DNS data; Bernardini & Pirozzoli (2011), compressible DNS data at $Re_\theta = 4300$.

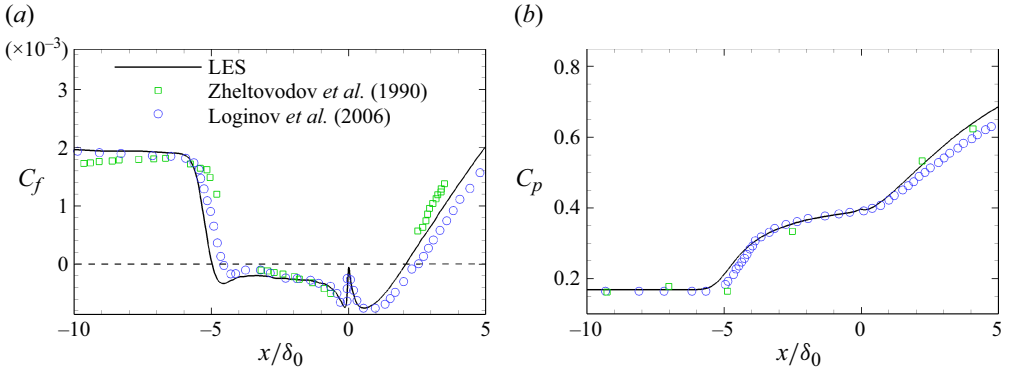

Figure 4. Distributions of (a) the skin-friction coefficient C_f and (b) the pressure coefficient C_p. Reported quantities are averaged over time and spanwise direction.

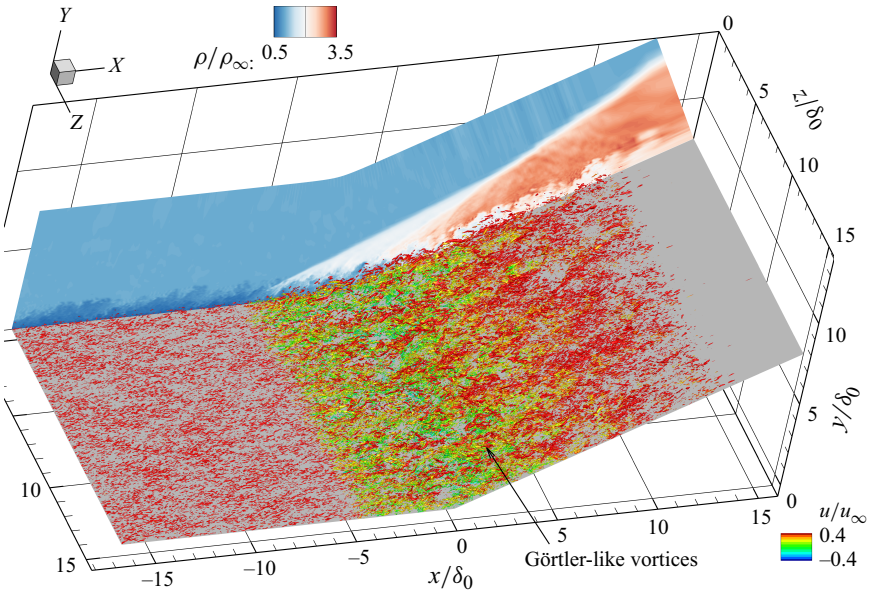

Figure 5. Instantaneous 3-D flow structures extracted using the Q criterion, coloured by streamwise velocity u/u_∞ from -0.4 to 0.4. The iso-surface value of Q is set to 5 % of its maximum. The contour in the x-y plane represents the density distribution.

and reattachment points. Overall, the present LES results agree well with previous LES results and experimental data. The current grid resolutions are adequate.

Instantaneous 3-D vortical structures identified using the Q criterion are shown in figure 5, along with the density contour in the x-y plane. Vortices are primarily generated near the shock foot and propagate downstream over the TSB. These vortices are in the form of streamwise vortices with a spanwise wavelength of approximately $2\delta_0$, referred to as Görtler-like vortices. Zhuang *et al.* (2017) also observed these Görtler-like vortices immediately downstream of the separation shock using a Rayleigh scattering technique. No apparent large-scale spanwise structures (generally larger than the Görtler-like vortices) are observed.

Spectral analysis is performed on wall-pressure signals. Welch's method (Welch 1967) is employed for spectral estimation, using a standard Hamming window to weight the data. The signals are divided into three segments with a 50 % overlap and the length of each segment is approximately $1500\delta_0/u_\infty$ ($214L_{sep}/u_\infty$). Figure 6 shows the spanwise-averaged spectrum of wall pressure as a function of Strouhal number $St = fL_{sep}/u_\infty$ along the streamwise direction. The mean separation line, corner and reattachment line are marked in the figure.

Upstream of the interaction region, the contour presents a broadband bump centred around $St = 5 - 7$, with no significant low-frequency content. This broadband bump corresponds to energetic scales in the undisturbed TBL. In the intermittent region, the energy is primarily concentrated in the low-frequency region, with a peak frequency of $St = 0.042$ and an intermittent length of approximately $2\delta_0$. The peak frequency falls within the range of $St = 0.02{-}0.05$ (Dussauge *et al.* 2006). Downstream of the interaction region, the energetic scales shift back to the high-frequency zone, although some low-frequency structures persist. Interestingly, Jenquin *et al.* (2023) identified a prominent peak in the frequency range $St = 0.2{-}0.4$ near the mean reattachment line, they concluded that it is the signature of Görtler-like structures. However, this peak is not evident in our

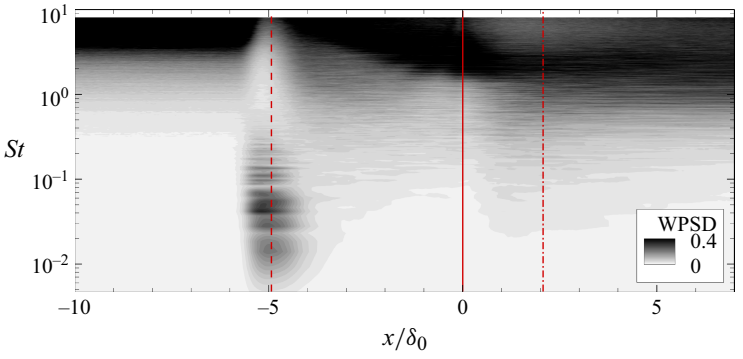

Figure 6. Contour of weighted power spectral density (WPSD) of wall-pressure signals. The dashed line indicates the mean separation point x_s, the dashed dotted line denotes the mean reattachment point x_r and the solid line marks the corner.

spectrum and in other simulations (Touber & Sandham 2009; Grilli *et al.* 2012; Priebe & Martín 2012; Pasquariello *et al.* 2017; Ceci *et al.* 2023), which needs further investigations in future studies.

3.2. *Evidence of large-scale spanwise motions*

3.2.1. *Proper orthogonal decomposition results*

Space-only POD is performed on wall pressure to examine potential spanwise structures surrounding the mean separation line. Figure 7(*a*,*b*) shows the leading POD mode and the mode energy distribution of the first 100 modes. Spanwise structures near the mean separation line can be observed in the mode, characterised by a large spanwise wavelength of the order of $O(15\delta_0)$. According to Ceci *et al.* (2023, 2024), the spanwise structures are signatures of the rippling of the separation line. Interestingly, $O(15\delta_0)$-scale structures with opposing signs emerge near the mean reattachment line. The correlation between the structures near the mean separation and reattachment lines indicates these structures may be associated with motions of the whole TSB. Most of the energy is captured by numerous high-order modes, with the leading mode occupying only approximately 1.2 % of the total energy. The low energy ratio may be attributed to extra acoustic disturbances arising at the inlet (Ceci *et al.* 2022). The cumulative energy of the first 100 POD modes accounts for 30 % of the total energy. Consequently, the motions surrounding the mean separation line are multimodally coupled and cannot be simply reconstructed using only the first few energetic modes.

A low-pass filter is commonly used to investigate the low-frequency dynamics in STBLIs, as noted by Priebe & Martín (2012) and Tong *et al.* (2017). Therefore, we apply a low-pass filter with a cutoff frequency $St_{cut} = 0.05$ to the raw wall pressure to isolate low-frequency fluctuations. This cutoff frequency is around the characteristic frequency band of the shock motions. Figure 7(*c*) displays the leading POD mode derived from the filtered wall pressure. Compared with the unfiltered leading POD mode, the spanwise structures near the mean separation and reattachment lines are nearly identical in shape and position, which indicates that the large-scale spanwise structures are primarily associated with the low-frequency dynamics. Figure 7(*d*) shows the corresponding energy distribution for the first 100 modes and the cumulative energy. The leading mode captures 25 % of the total energy, exhibiting a low-rank feature. The first 40 POD modes collectively account for nearly 100 % of the total energy. It is clear that the low-pass filter effectively removes high-frequency components while preserving low-frequency large-scale structures. The leading

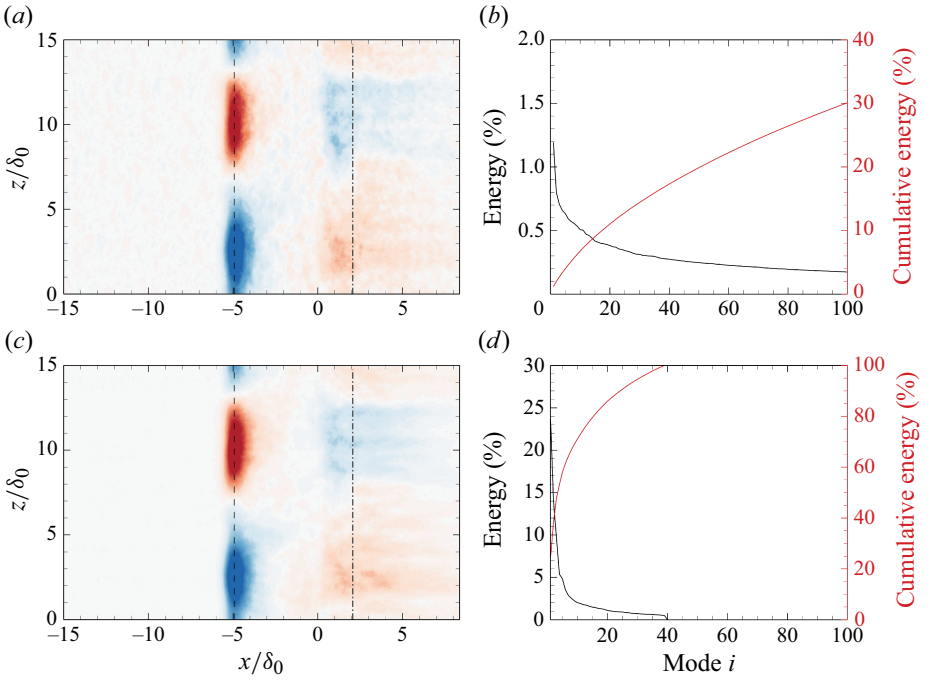

Figure 7. (*a*) Leading POD mode and (*b*) corresponding energy distribution of the first 100 POD modes from the raw wall-pressure signals; (*c*) filtered (low-pass filter, $St_{cut} = 0.05$) leading POD mode and (*d*) its associated energy distribution of the first 100 POD modes. The dashed lines in (*a*,*c*) indicate the mean separation point x_s, while the dash dot lines represent the mean reattachment point x_r.

POD modes shown in figure 7(*a*,*c*) resemble those observed in the non-swept case noted by Ceci *et al.* (2023, 2024).

3.2.2. *Spectral proper orthogonal decomposition results*

Spectral proper orthogonal decomposition is then applied to extract coherent structures based on the LES data. A segment length of $1500\delta_0/u_\infty$ with a 90 % overlap is used, leading to 11 realisations. A standard Hamming window is applied to minimise spectral leakage. It is noted that the results are nearly identical when using a Hann window or a relatively short segment of $1300\delta_0/u_\infty$. Figure 8(*a*) presents the normalised SPOD eigenvalues at station x_3 ($x = 0$, at the corner). The energy decreases with increasing frequency across different modes. The dominant frequency for mode 1 is the lowest resolvable frequency, $St = 0.0046$. This frequency is almost an order of magnitude lower than the quasi-2-D shock motion frequency $St = 0.02 - 0.05$ (Dussauge *et al.* 2006). The normalised eigenvalues of the SPOD modes at $St = 0.0046$ are depicted in figure 8(*b*). The optimal mode is significantly more energetic than the other, capturing 61 % of the total energy. This indicates the presence of low-rank features in the dynamical system in the spanwise direction at this frequency.

Figure 9 depicts three velocity components of the leading SPOD mode at $St = 0.0046$ at station x_3. From the streamwise velocity perturbation $\hat{u}$, two types of coherent structures located at different wall-normal locations are observed: large-scale spanwise structures of $O(15\delta_0)$ surrounding the separation shock (referred to as the shock component) and structures near the wall (referred to as the near-wall component). The near-wall component seems to contain structures with spanwise wavelengths of both $O(15\delta_0)$ and $O(2\delta_0)$,

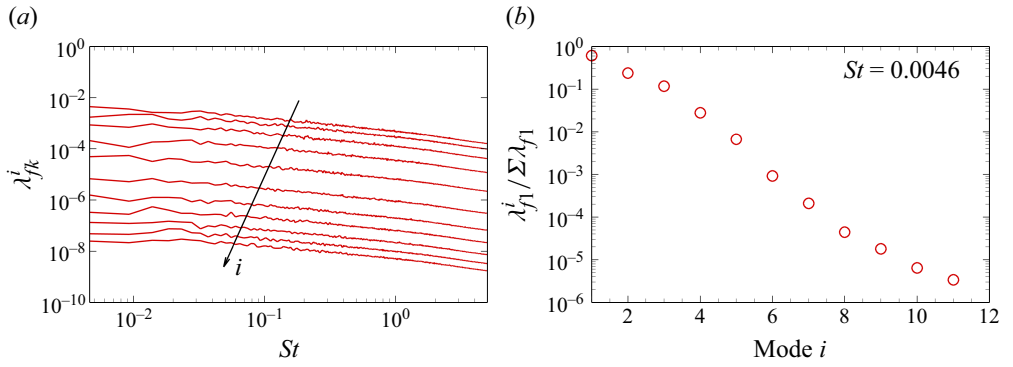

Figure 8. At station x_3: (*a*) SPOD eigenvalues as a function of frequency, normalised by the total flow energy; (*b*) SPOD eigenvalues at the lowest frequency $St = 0.0046$, normalised by the total flow energy at this frequency.

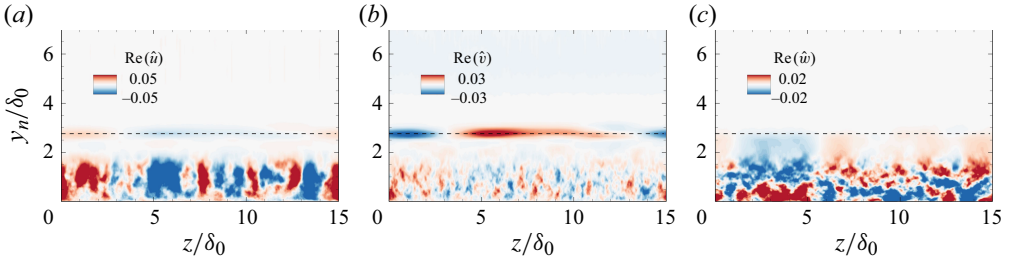

Figure 9. Real parts of (*a*) $\hat{u}$, (*b*) $\hat{v}$ and (*c*) $\hat{w}$ of the leading SPOD mode at $St = 0.0046$ at station x_3. The black dashed lines indicate the separation shock locations and y_n is the wall-normal distance.

while the large-scale structures are modulated by the Görtler-like vortices immediately downstream of separation point, as shown in figure 5. Similar modulation effects between structures of different scales inside TSBs have also been documented by Borgmann *et al.* (2024). For the vertical velocity perturbation $\hat{v}$, most fluctuations are attributed to the shock component, while the near-wall component can be barely seen. The near-wall structures remain evident in the spanwise velocity perturbation $\hat{w}$, whereas the shock component is not present around the separation shock but is located beneath it.

Figure 10 (*a*,*c*,*e*) presents the leading SPOD modes at stations $x_1 - x_5$ at $St = 0.0046$, along with the iso-lines of $\bar{u}/u_\infty = 0.99$ that mark the separation shock. At station x_1 (within the intermittent region), the two components merge into a common large-scale spanwise structure. Downstream of x_1, the coherent structures at different stations resemble those in figure 9 and maintain the two components. The shock components remain of the order of $15\delta_0$ in the spanwise direction, suggesting the presence of persistent large-scale structures. The near-wall components remain modulated by Görtler-like structure up to x_5, where modulation ceases and Görtler-like vortices become dominant. These near-wall structures at x_5 in figure 10 (*a*) resemble the turbulent Görtler vortices reported by Zhang, Hao & Uy (2025), which are characterised by counter-rotating pairs.

A clear streamwise evolution of the two types of structures is shown in figure 10(*b*,*d*,*f*), which presents the leading SPOD mode in the mid-span plane at $St = 0.0046$. The perturbation $\hat{u}$ is excited near the shock foot and develops into the shock and near-wall components. The two components correspond to the two components in the spanwise

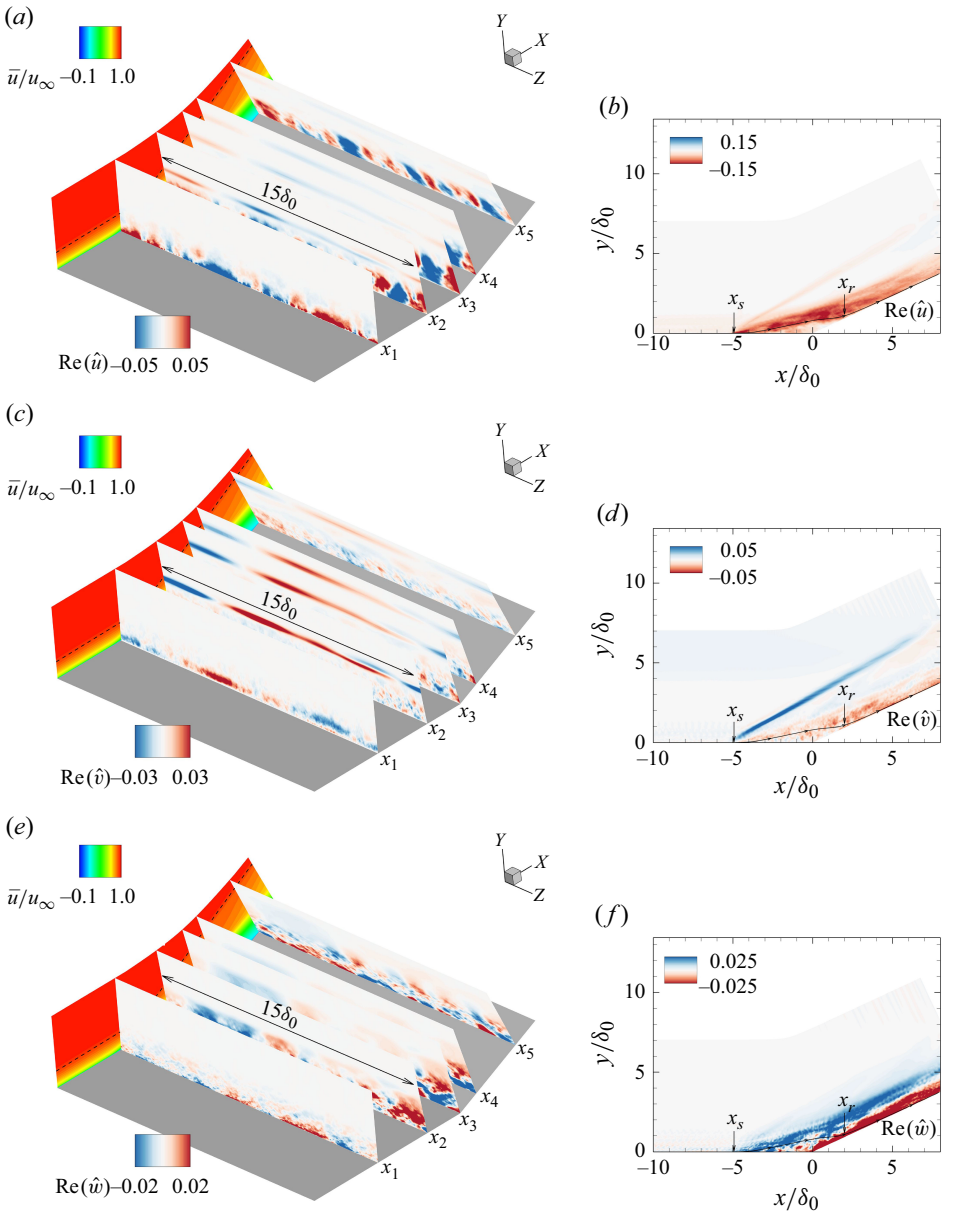

Figure 10. Real parts of (a,b) $\hat{u}$, (c,d) $\hat{v}$ and (e,f) $\hat{w}$ of the leading SPOD modes at $St = 0.0046$. (a,c,e) Results for the y-z planes at stations $x_1 - x_5$; (b,d,f) results for the mid-span plane. The mean streamwise velocity contours on the x-y plane through $z/\delta_0 = 0$ are shown in (a,c,e), along with black dashed lines indicating the iso-lines of $\overline{u}/u_\infty = 0.99$. The streamlines in (b,d,f) pass through the point $(x_s, 0.01\delta_0)$.

direction shown in figure 10(a,c,e). The near-wall component continues along both the separation bubble and the reattached boundary layer. In contrast, the shock component persists solely along the shock. Furthermore, $\hat{u}$ keeps nearly the same sign throughout the computational domain. Most of $\hat{v}$ is concentrated along the separation shock, with only slight fluctuations occurring close to the wall. The sign of $\hat{w}$ changes inside the separation bubble.

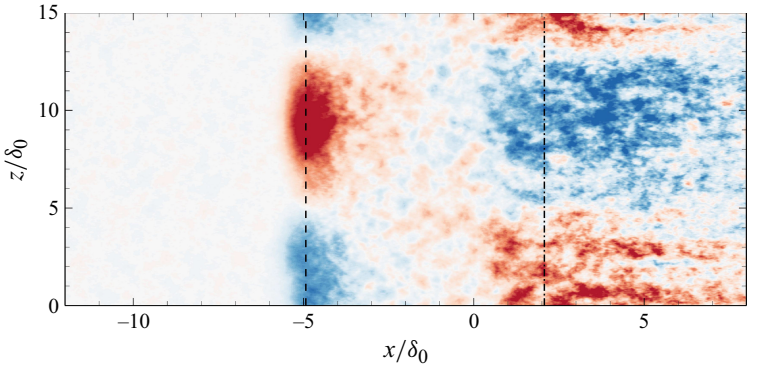

Figure 11. Real part of the leading SPOD mode of wall pressure at $St = 0.0046$. The dashed line indicates the mean separation point x_s, the dashed dot line denotes the mean reattachment point x_r.

Figure 11 presents the real part of the leading SPOD mode of wall pressure at $St = 0.0046$. As expected, the large-scale spanwise structures are observed surrounding the mean separation line, consistent with the leading POD modes in figures 7(*a*,*c*). Furthermore, similar large-scale spanwise structures with opposite signs also appear near the mean reattachment point x_r, though these are less organised than those near x_s. This irregularity is likely caused by the near-wall Görtler-like vortices, which modulate the large-scale spanwise structures near x_r. The corresponding relationship between structures at x_s and x_r indicates that the spanwise rippling may be associated with the entire TSB motions. Combined with the observation of shock rippling at various streamwise locations, this leads to the following hypothesis: the TSB motions induce the rippling of the separation line, which, in turn, causes the rippling of the separation shock. The dynamics of this system is elaborated later.

All in all, the SPOD method successfully extracts the low-frequency coherent structures in the spanwise direction which are excited near the shock foot and persist along the separation shock. These structures manifest as spanwise rippling, with wavelengths of the order of $O(15\delta_0)$.

3.3. *Influence of spanwise width*

To confirm that the captured $15\delta_0$ ($2L_{sep}$) structures are not artefacts arising from spanwise domain constraints, a larger domain width of $L_z = 30\delta_0$ ($\approx 4L_{sep}$) is adopted. A coarser mesh is used in the x and z directions to save the computational cost, with resolutions of $\Delta x^+ \approx 30$, and $\Delta z^+ \approx 15$. The total physical time is reduced to $1300\delta_0/u_\infty$.

The SPOD analysis is performed on y-z planes at different streamwise stations and on wall-pressure signals. The segment length is $650\delta_0/u_\infty$, with a 90 % overlap. Figure 12 shows the leading SPOD modes at the lowest frequency $St = 0.0096$ at stations x_2, x_3, x_4 and x_5. These modes consist of a near-wall component and a large-scale shock component, resembling the leading modes in figure 10(*a*,*c*). Two pairs of large-scale spanwise structures surrounding the separation shock are observed at different stations, with a wavelength approximately $\lambda_z = 15\delta_0$ ($\approx 2L_{sep}$). The wavelength and mode shape align well with those captured in the relatively narrow computational domain ($15\delta_0$), confirming domain-size independence.

Furthermore, figure 13 presents the leading SPOD mode at $St = 0.0096$ for wall-pressure fluctuations. Consistent large-scale spanwise structures are observed around the mean separation line, accompanied by opposing-sign structures near the reattachment line.

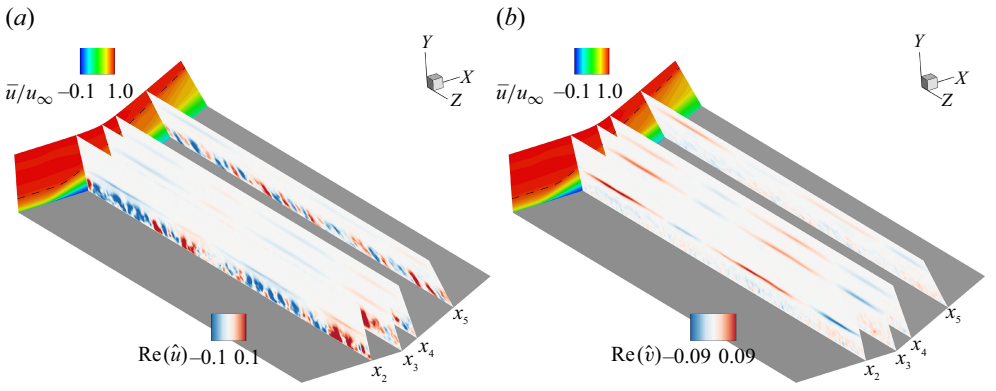

Figure 12. Real parts of (*a*) $\hat{u}$ and (*b*) $\hat{v}$ of the leading SPOD modes at $St = 0.0096$ at stations x_2, x_3, x_4, x_5 for the $30\delta_0$ case and the mean streamwise velocity contour on an x-y plane through $z/\delta_0 = 0$. The black dashed line on the x-y plane indicates the iso-line of $\bar{u}/u_\infty = 0.99$.

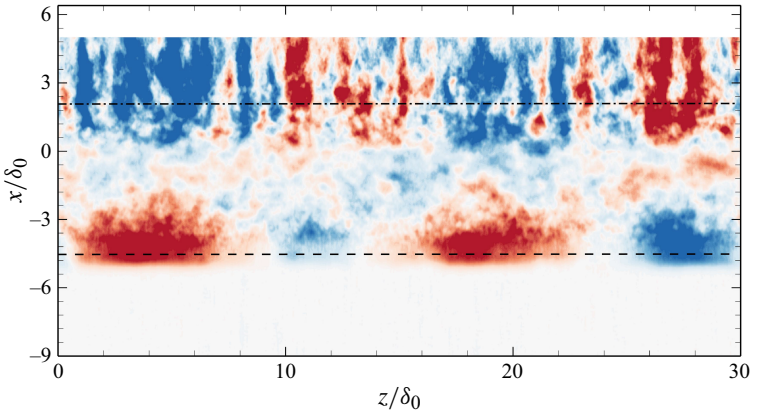

Figure 13. Real part of the leading SPOD mode of wall pressure at $St = 0.0096$ from the $30\delta_0$ case. The dashed line indicates the mean separation point x_s, the dashed dot line denotes the mean reattachment point x_r.

The spatial coherence between the leading SPOD modes across streamwise stations and wall-pressure data confirms that these structures are physical features rather than numerical artefacts.

4. Discussion

4.1. *Origins of large-scale spanwise motions*

A GSA is conducted to investigate potential global modes of the dynamical system associated with the TSB. Figure 14 shows the most unstable modes at different wavenumbers $\beta\delta_0$. As the wavenumber increases, the growth rates rise to the peak at $\beta\delta_0 = 0.43$ and subsequently decline, becoming stable when $\beta\delta_0$ exceeds 1.1. The wavelength of the peak roughly corresponds to $\lambda_z \approx 15\delta_0$, which justifies the choice of L_z. Furthermore, all these modes are stationary with $\omega_r = 0$. Zero-frequency globally unstable modes indicate that small perturbations will grow exponentially without oscillations until nonlinear saturation.

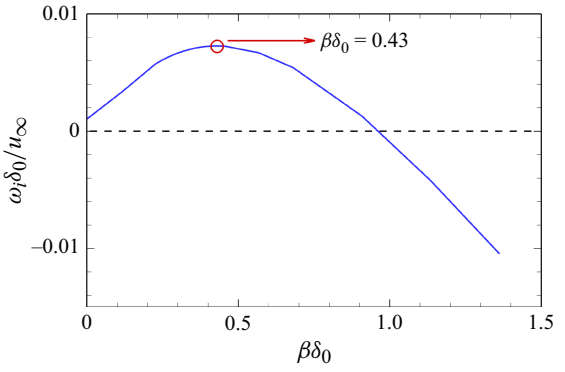

Figure 14. The most unstable modes at different wavenumbers $\beta\delta_0$. The black dashed line indicates zero growth rate.

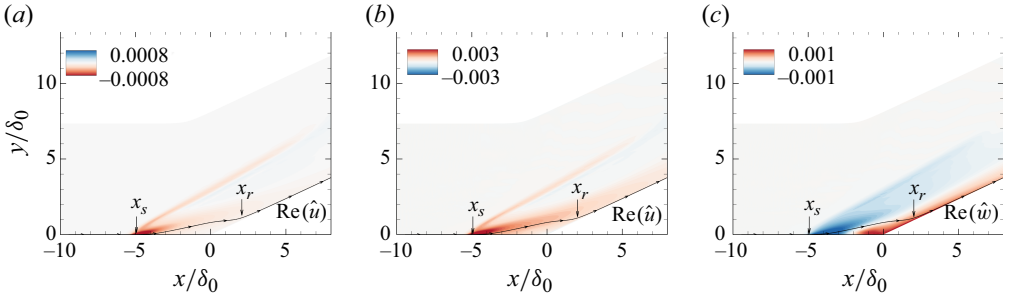

Figure 15. Real part of (*a*) $\hat{u}$ of the shock mode ($\beta\delta_0 = 0.0$), (*b*−*c*) $\hat{u}$ and $\hat{w}$ of the bubble mode ($\beta\delta_0 = 0.43$). The streamlines pass through the point (x_s, $0.01\delta_0$).

Note that the GSA modes are normalised using the L_2 norm. Consequently, only the relative spatial distributions within each mode are physically meaningful. The eigenfunctions of the 2-D mode (referred to as the shock mode) is shown in figure 15(*a*). The streamwise velocity perturbation $\hat{u}$ is predominantly concentrated around the shock foot and the separation shock. Downstream of the shock foot, $\hat{u}$ diminishes and becomes barely visible within the separation bubble. Nichols *et al.* (2017) and Hao (2023) captured similar 2-D shock modes that were thought to contribute to low-frequency shock motions, but this mode is not the focus of our study.

Of particular interest is the most unstable 3-D mode (referred to as the bubble mode) shown in figure 15(*b*−*c*). Two-component structures appear in this mode: one along the separation shock and another near the wall. Unlike the shock mode, $\hat{u}$ remains at a high level within the separation bubble and downstream of the corner. Additionally, $\hat{u}$ maintains the same sign throughout the computational domain, while $\hat{w}$ exhibits sign reversal beneath the shear layer. The characteristics of both the shock mode and the bubble mode align well with previous RANS-based GSA results (Hao 2023), which indicate that the linear dynamics of TSBs are largely insensitive to turbulence modelling.

Qualitatively, the eigenfunction of the bubble mode resembles the leading SPOD mode of the mid-span plane presented in figure 10(*b*, *f*), exhibiting a similar streamwise evolution of the two components. The quantitative comparison of the two modes is made using their projection, given by

$$\gamma = \frac{\left| \| \hat{\boldsymbol{\Psi}}_{\boldsymbol{SPOD}}(x, y),\ \hat{\boldsymbol{Q}}_{\boldsymbol{GSA}}(x, y) \|_E \right|}{\| \hat{\boldsymbol{\Psi}}_{\boldsymbol{SPOD}}(x, y) \|_E \times \| \hat{\boldsymbol{Q}}_{\boldsymbol{GSA}}(x, y) \|_E}, \tag{4.1}$$

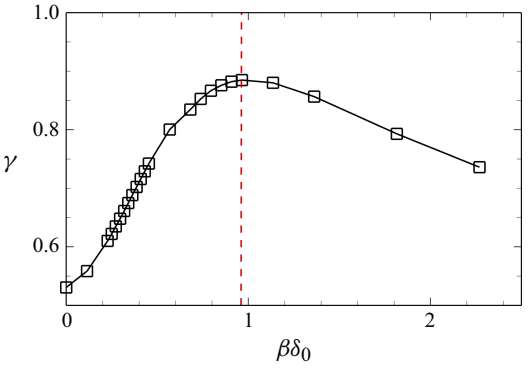

Figure 16. The projection coefficient between the leading SPOD mode of the mid-span plane at $St = 0.0046$ and the global modes over various spanwise wavenumbers. The red dashed line indicates the local maximum $\beta\delta_0 = 0.96$.

where $\hat{\boldsymbol{\Psi}}_{\boldsymbol{SPOD}}(x, y)$ represents the leading SPOD mode, while $\hat{\boldsymbol{Q}}_{\boldsymbol{GSA}}(x, y)$ denote the GSA modes over several spanwise wavenumbers. The notation $\|\cdot\|_E$ denotes the Chu norm (Chu 1965). A value of $\gamma = 0$ indicates orthogonality between the two modes, while $\gamma = 1$ signifies perfect alignment (Abreu *et al.* 2020). It should be noted that $\hat{\boldsymbol{\Psi}}_{\boldsymbol{SPOD}}(x, y)$ aggregates structures at different wavenumbers implicitly, whereas $\hat{\boldsymbol{Q}}_{\boldsymbol{GSA}}(x, y)$ represents structures at a specific wavenumber. Consequently, the projection can illustrate the similarities between the two types of modes and identify the wavenumber of dominant structures through the peak $\gamma(\beta\theta_0)$. Cura *et al.* (2024) applied a similar projection strategy to compare the optimal SPOD mode (derived from planar PIV data) with resolvent modes at different wavenumbers.

Figure 16 depicts the projection coefficient as a function of spanwise wavenumbers. The projection coefficient increases to a peak at $\beta\delta_0 = 0.96$ and then decreases as $\beta\delta_0$ continues to increase. The peak value is $\gamma = 0.88$, which indicates a strong alignment between the two modes. The small discrepancy in the peak wavenumber primarily arises from the different wavelengths of the near-wall component from GSA and SPOD. The GSA models perturbations as $15\delta_0$ coherent structures for both shock and near-wall components, while the near-wall Görtler-like vortices are approximately $2\delta_0$ in SPOD. The difference in wavelength leads to a decrease in the peak value of γ and an increase in the wavenumber of the peak γ.

The spanwise structures of the two components from SPOD and GSA are then examined. For ease of comparison, figure 17 presents a comparison of the leading SPOD modes shown in figure 10 and the reconstructed 3-D perturbations using the bubble mode at the same stations $x_1 - x_5$. Qualitatively, the shock components of the bubble mode resemble the coherent structures surrounding the separation shock in the SPOD modes, especially in terms of origin and development path. However, the near-wall component of the perturbations from the bubble mode is not fully reflected in the leading SPOD modes. The centrifugal effects dominate over the global instability near the wall, leading to the modulating effects of the Görtler-like structures on the near-wall spanwise mode of $O(15\delta_0)$. The effects of global instability are concentrated mainly near the shock foot and along the separation shock. It should be noted that the biased shock components observed in SPOD may be caused by nonlinear effects. Moreover, the bubble mode is stationary, indicating an extremely low characteristic frequency, which is also a key feature of the leading SPOD modes, as previously mentioned.

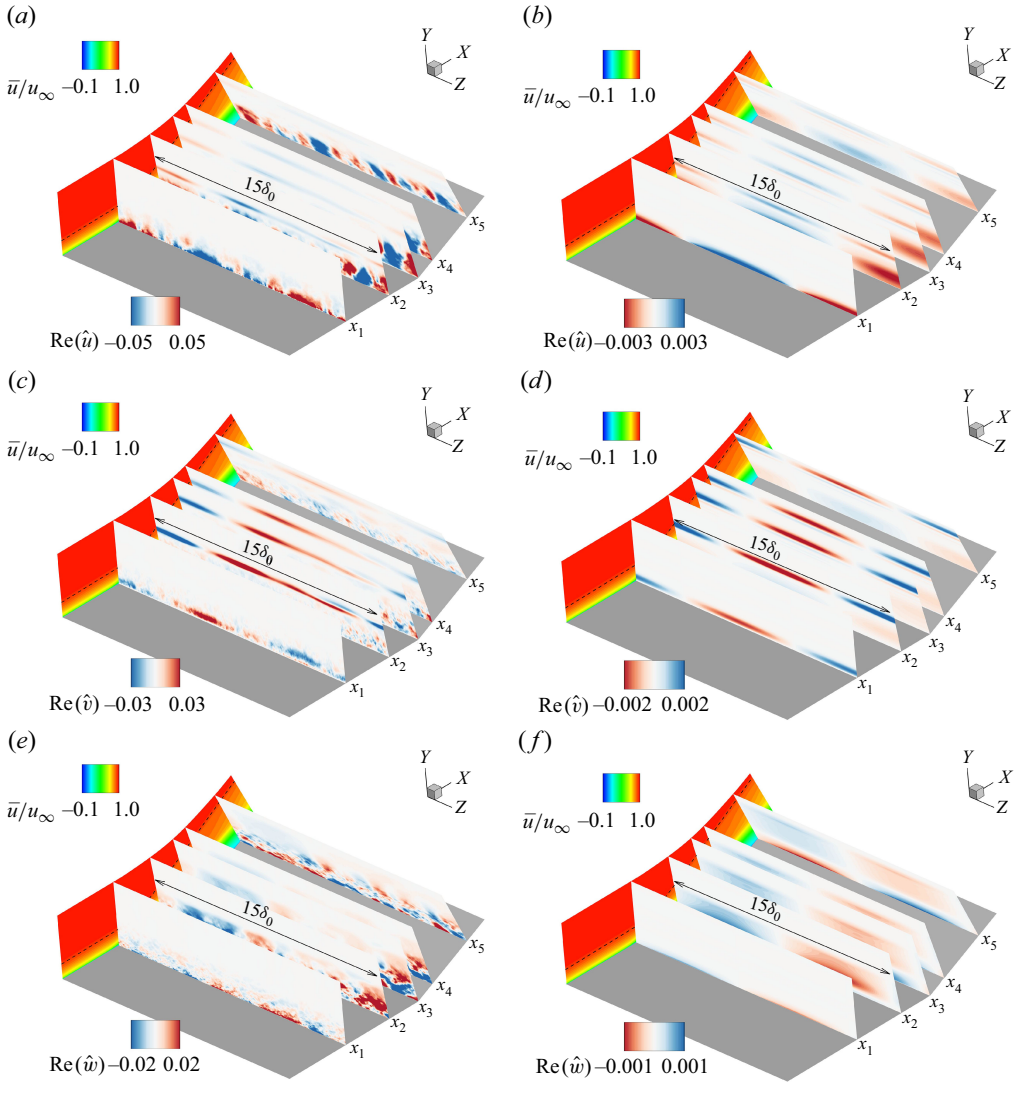

Figure 17. Comparisons of the leading SPOD modes (a,c,e) at $St = 0.0046$ and reconstructed 3-D perturbations (b,d,f) using the bubble mode at stations $x_1 - x_5$.

Figure 18 compares the distributions of the spanwise-averaged Chu energy density along the wall-normal direction for the leading SPOD modes at $St = 0.0046$ and the bubble mode at stations x_2, x_3 and x_4. The Chu energy density is used to represent fluctuating energy distribution along the wall-normal direction, defined as

$$\text{Chu energy density} = \bar{\rho}|\mathbf{u}'|^2 + \frac{\bar{T}}{\bar{\rho}\gamma {M_\infty}^2}(\rho')^2 + \frac{\bar{\rho}}{(\gamma-1)\gamma {M_\infty}^2 \bar{T}}(T')^2, \tag{4.2}$$

where $\mathbf{u} = [u, v, w]^T$. The trends of Chu energy density at different stations are similar, with a first peak close to the wall and a second peak near the shock. The shock components from SPOD and GSA are almost identical, while the near-wall components show significant differences in both strength and position, particularly at station x_4. These discrepancies are attributed to the modulation effects of the Görtler-like structures. Despite

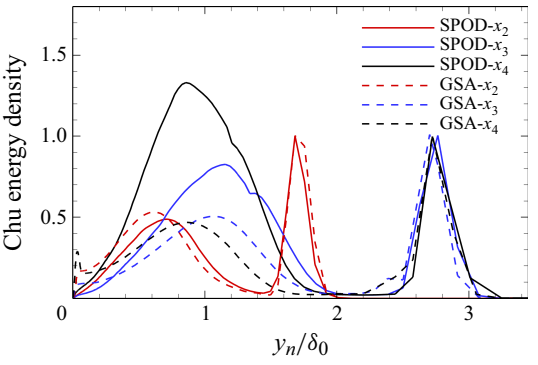

Figure 18. Wall-normal distributions of the spanwise-averaged Chu energy density from the leading SPOD modes at $St = 0.0046$ and the bubble mode at stations x_2, x_3 and x_4 normalised by their respective maximum values near the separation shock.

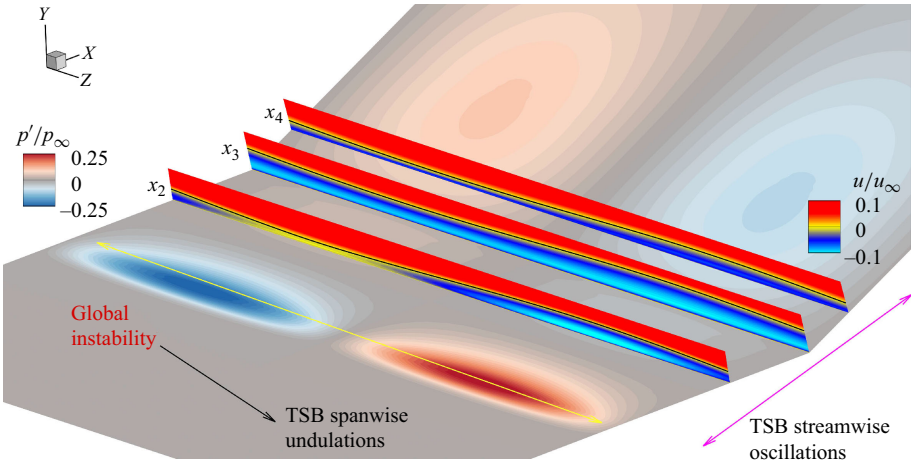

Figure 19. Reconstructed perturbed flow field using the bubble mode from (2.1), superimposed with wall-pressure fluctuations. The y-z slices are located at stations x_2, x_3 and x_4, with black lines denoting $u/u_\infty = 0$.

the near-wall differences, the similarities near the separation shock indicate that large-scale spanwise structures captured by SPOD are consistent with those detected by GSA.

Qualitative and quantitative comparisons are made between GSA and SPOD results to demonstrate that the spanwise rippling captured by SPOD primarily arise from global instability. Recall the hypothesis given in § 3.2.2 that the spanwise undulations of the TSB are suspected to be the direct cause of the rippling. To model the spanwise motions of the TSB influenced by global instability, we reconstruct a perturbation field $\boldsymbol{Q'}$ superimposed with the 2-D mean flow $\boldsymbol{Q_{2-D}}$, as illustrated in figure 19. The perturbation field $\boldsymbol{Q'}$ is reconstructed using (2.3). The time factor is simplified as a constant by setting $|\hat{w}|_{max}/u_\infty = 0.05$, which is appropriate for the TSB shape.

At different stations, the TSB size varies in the spanwise direction, exhibiting peaks and valleys. These spanwise variations are attributed to the TSB undulations, consistent with the reconstruction by Borgmann *et al.* (2024) using a low-order model. The dynamical system associated with the TSB is summarised as follows. As the TSB oscillates in the streamwise direction, it also experiences spanwise undulations due to global instability.

	M_∞	Re_{δ_0}	Interaction type	Spanwise scale
Ceci *et al.* (2023)	2.28	15800	Shock impingement	$2L_{sep}$
Dau *et al.* (2023)	0.09	10000	Hump	$0.8L_{sep}$
Jenquin *et al.* (2023)	2.5	185500	Compression ramp	–
Liu *et al.* (2024)	2.83	98600	Compression ramp	–
Ceci *et al.* (2024)	5.0	55474	Shock impingement	$2L_{sep}$
Present case	2.95	63500	Compression ramp	$2L_{sep}$

Table 2. Summary of studies reporting large-scale spanwise structures. The symbol – indicates the observations of large-scale spanwise pressure fluctuations near the mean separation line in these studies; however, quantitative characterisation of the most energetic spanwise structures (e.g. dominant scales) caused by TSB motions is not given explicitly.

These undulations affect the separation shock, causing its motion to become spanwise-dependent rather than purely two-dimensional. As a result, the shock undergoes similar spanwise undulations, which correspond to the large-scale spanwise structures identified using SPOD in figure 10. The rippling serves as an intuitive representation of the spanwise undulations of the TSB. Furthermore, the opposite-sign large-scale wall-pressure fluctuations are consistent with the POD modes in figure 7(a,c) and leading SPOD mode in figure 11.

Flow conditions for the present case and prior studies reporting large-scale spanwise structures are summarised in table 2. The free-stream parameters and interaction types vary across these cases, spanning subsonic to hypersonic regimes. While spanwise undulations of TSBs have been observed in reported cases, other works report no such modes. Three potential factors may explain this discrepancy. First, many prior STBLI investigations employed narrow spanwise domains (typically $4\delta_0-6\delta_0$), which may inadequately resolve large-scale spanwise motions. Second, the emergence of these motions may critically depend on free-stream parameters such as Mach number, temperature ratio and Reynolds number. Third, the separation scales (or the interaction strengths) may influence the manifestation of such spanwise modes. For example, the linear bubble dynamics may dominate in strongly separated flows, whereas other convective linear dynamics may prevail in weakly separated flows. Our present study focuses solely on one case; therefore, we do not assert generality. Future work will systematically investigate the influence of parameters, including the Mach number, Reynolds number, temperature ratio and interaction strength, to determine whether such bubble modes are intrinsic.

4.2. *Coupling of spanwise unsteadiness and quasi-2-D streamwise motions*

In previous STBLI studies focusing on the low-frequency unsteadiness in 2-D interactions (e.g. compression ramp and shock impingement), the shock motions are usually modelled as nominally 2-D structures, as summarised by Clemens & Narayanaswamy (2014). The standard methodology for analysing the 2-D dynamics is to average flow variables in the spanwise direction, as implemented by Grilli *et al.* (2012), Priebe & Martín (2012), Priebe *et al.* (2016) and Pasquariello *et al.* (2017). However, this quasi-2-D framework inherently excludes low-frequency spanwise unsteadiness, which remains unaccounted for in such simplified models. Here, the spanwise unsteadiness and streamwise oscillations are investigated to characterise their interplay, providing insights into 3-D bubble motions.

Given that the characteristic frequency of quasi-2-D shock motions lies around $St = 0.02-0.05$ (Dussauge *et al.* 2006), and the spanwise undulations of TSBs are characterised by a very low-frequency dynamics, the range $St = 0.0-0.05$ can encompass both types

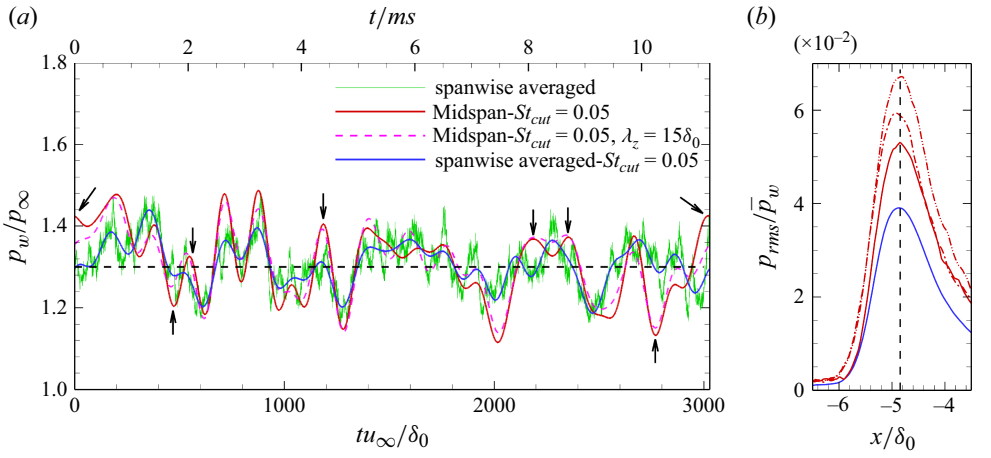

Figure 20. (*a*)Four wall-pressure signals at x_s: spanwise averaged (unfiltered), frequency filtered and spanwise averaged ($St_{cut} = 0.05$), frequency-filtered mid-span ($St_{cut} = 0.05$) and frequency- and wavelength-filtered mid-span ($St_{cut} = 0.05$, $\lambda_z = 15\delta_0$). The black arrows indicate some opposite motions between the filtered spanwise-averaged and filtered mid-span signals. (*b*) Normalised r.m.s. of the frequency-filtered spanwise-averaged pressure signal (blue) and three frequency-filtered wall-pressure signals within the intermittent region at $z/\delta_0 = 3.75$ (dash dot), 7.5 (red solid) and 11.25 (dash dot dot). The black dashed line in (*a*) denotes the mean value $p_w/p_\infty = 1.3$ at x_s, and in (*b*) indicates x_s.

of oscillations. To capture these dynamics, a low-pass filter with a cutoff frequency $St_{cut} = 0.05$ is employed to the raw and spanwise-averaged wall-pressure signals. Since the streamwise oscillations of the shock foot result in sharp increases or decreases in wall pressure near x_s, the instantaneous pressure fluctuations can effectively represent the shock motions. Importantly, these shock motions are indicative of the TSB motions. Therefore, the instantaneous pressure fluctuations also serve as a marker for the TSB motions.

Figure 20(*a*) compares four wall-pressure signals at the location x_s: the spanwise-averaged signal, the frequency-filtered spanwise-averaged signal ($St_{cut} = 0.05$), the frequency-filtered mid-span signal ($St_{cut} = 0.05$) and the frequency- and wavelength-filtered mid-span signal ($St_{cut} = 0.05$, $\lambda_z = 15\delta_0$). Wavelength filtering is achieved by performing a discrete Fourier transform on the frequency-filtered spanwise pressure distribution to isolate the specific $\lambda_z = 15\delta_0$ component. The mid-span signal is then reconstructed from this wavelength-specific mode. The frequency-filtered spanwise-averaged signal primarily reflects quasi-2-D oscillations, while the frequency-filtered mid-span signal captures a combination of both spanwise and streamwise motions. The trends of both frequency-filtered signals are similar most of the time, which indicates that the streamwise shock motions remain dominant. However, at certain moments, the two pressure signals diverge and appear on opposite sides of the line $p_w/p_\infty = 1.3$, as marked in the black arrows in the figure. The frequency- and spanwise-filtered mid-span signal almost overlaps with the frequency-filtered signal, which indicates the dominant contribution of the $15\delta_0$ spanwise undulations to the marked opposing pressure fluctuations. Figure 20(*b*) shows a comparison between the r.m.s. values of the frequency-filtered spanwise-averaged signal and three frequency-filtered signals at $z/\delta_0 = 3.75$, 7.5 and 11.25. The peak r.m.s. value from the filtered spanwise-averaged signal is lower than those from the three filtered signals, accounting for approximately 66 %, 74 % and 58 % of their respective peak r.m.s. values. The mean ratio of the r.m.s. at x_s in the spanwise direction is approximately 65 %. This high percentage highlights the dominant role of streamwise motions in the 3-D shock dynamics.

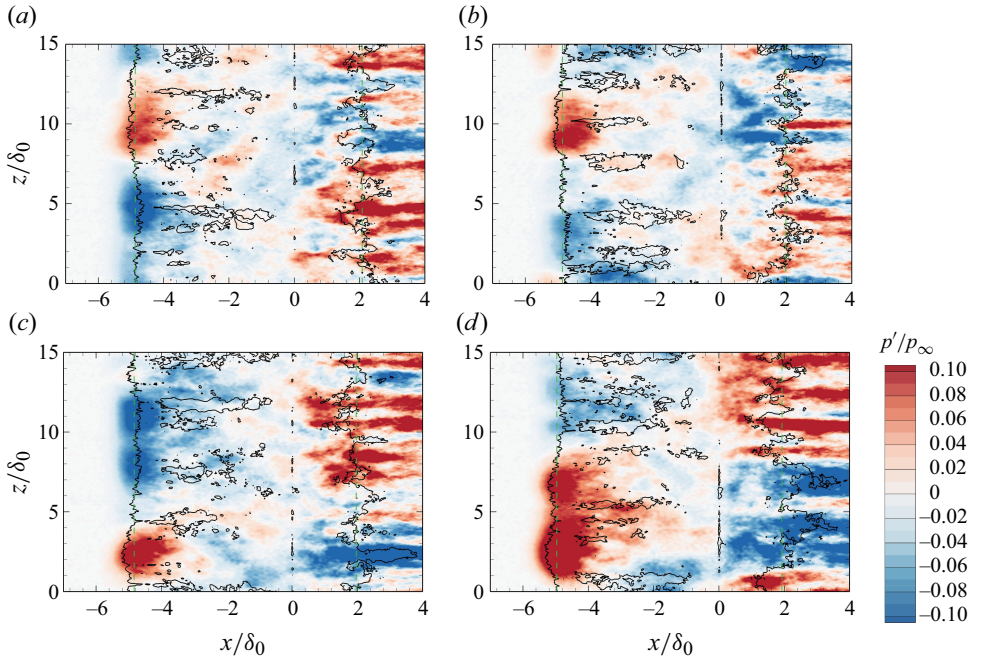

Figure 21. Time sequence of filtered wall-pressure fluctuations, normalised by the free-stream pressure, over a duration of 1.92 ms: (*a*) $t = 0.128$ ms, (*b*) $t = 0.768$ ms, (*c*) $t = 1.408$ ms and (*d*) $t = 2.048$ ms. The black lines denote the filtered iso-lines of $C_f = 0$, while the green dashed lines represent the filtered spanwise-averaged iso-lines of $C_f = 0$. The cutoff frequency is $St_{cut} = 0.05$.

Figure 21 presents the time sequence of filtered wall-pressure fluctuations over a duration of 1.92 ms (long-time evolution is shown in the Supplementary movie). The filtered iso-lines of $C_f = 0$ (marked in black solid lines) and the filtered spanwise-averaged iso-lines of $C_f = 0$ (marked in green dashed lines) indicate 3-D large-scale spanwise undulations and quasi-2-D motions of the TSB, respectively. At different time instants, the black lines contract and expand accompanying the green lines simultaneously in the streamwise direction, which implies that both quasi-2-D breathing and spanwise rippling are active. Furthermore, the black lines surround the green lines, with the spanwise rippling corresponding to significant large-scale spanwise pressure fluctuations of approximately $15\delta_0$. These fluctuations indicate that, although the TSB oscillates integrally in the streamwise direction, the spanwise rippling still causes locally opposing pressure fluctuations, as shown in figure 20(*a*). The maximum streamwise distance between the two lines at $t = 2.048$ ms is approximately $0.5\delta_0$. This value is appreciable and occupies approximately 25 % of the intermittent region. These large-scale pressure fluctuations are consistent with previous experimental studies (Jenquin *et al.* 2023; Liu *et al.* 2024) and are responsible for the modes in figure 7(*a*,*c*) and figure 11.

Similarly, dominant large-scale spanwise pressure fluctuations persist around the 2-D reattachment lines. These fluctuations exhibit opposite signs relative to those near the separation lines, consistent with both the optimal SPOD mode shown in figure 11 and the GSA bubble mode in figure 19. The irregularities of the filtered reattachment lines and the small-scale streamwise streaks of pressure fluctuations are attributed to Görtler-like structures.

Our results demonstrate that streamwise oscillations and spanwise undulations of the TSB coexist, with streamwise motions dominating over spanwise motions. However, the

observed 65 % dominance ratio may not hold universally. Future studies will therefore investigate additional configurations to further quantify the roles of the two motions.

One may argue that the large-scale spanwise structures of the TSB are caused by the Görtler-like vortices. However, our results demonstrated that the GSA bubble mode primarily drives the large-scale spanwise oscillations of the TSB. The influence of the Görtler-like vortices on the large-scale spanwise structures near the reattachment lines is limited at $St < 0.05$, manifesting only as slight spanwise irregularities. In contrast, such irregularities are absent in the structures near the separation line. Moreover, perturbations originating from the Görtler-like structures can propagate both upstream and downstream, potentially influencing the shock system. However, at different streamwise locations, the shock components exhibit similar structures and spanwise wavelengths, suggesting that the Görtler-like structures have minimal impact on the large-scale spanwise structures. Overall, there is no direct evidence to suggest that the spanwise motions of the TSB are driven by Görtler-like vortices.

5. Conclusions

Large-scale spanwise structures in STBLIs over a 25° compression ramp at Mach 2.95 are investigated using LES. The leading POD mode of wall pressure within the intermittent region exhibits a distinct spanwise corrugation centred on the mean separation line, with a wavelength of $O(15\delta_0)$ or $O(2L_{sep})$. When a low-pass filter with $St_{cut} = 0.05$ is applied, the leading POD mode retains a similar structure and wavelength, which indicates that it is primarily associated with low-frequency motions. The SPOD method is employed to extract coherent structures in the spanwise direction from the LES database. At different streamwise stations, the leading SPOD modes of the y-z planes are characterised by low-frequency features. These modes consist of two components: the shock components with large-scale spanwise structures and the near-wall components. The shock components are excited near the shock foot and sustain along the separation shock, while the near-wall structures seem to be modulated by the Görtler-like vortices.

The GSA identifies a 3-D stationary bubble mode at a spanwise wavelength of $15\delta_0$. Qualitative and quantitative comparisons between the leading SPOD modes and the GSA bubble mode are conducted. Qualitatively, the streamwise evolution and spanwise scales of the shock components observed in the SPOD modes closely resemble those predicted by the bubble mode. Quantitatively, the peak projection coefficient between the leading SPOD mode in the mid-span plane and the bubble mode is as high as 0.88, which strongly indicates a high degree of alignment between the two modes. Furthermore, the Chu energy density distribution trends at different streamwise stations derived from the leading SPOD modes align well with those from the bubble mode, particularly near the separation shock. The qualitative and quantitative evidence significantly suggest that global instability is primarily responsible for the observed large-scale spanwise coherent structures. The reconstructed TSB using the 3-D bubble mode exhibits spanwise undulations, which directly cause the rippling of the shock. The dynamical system of the TSB can be summarised as follows: global instability induces spanwise undulations of the TSB, which in turn excite large-scale spanwise structures along the separation shock.

The coupling of shock motions in the spanwise and streamwise directions is also examined using filtered wall-pressure signals with a cutoff frequency $St_{cut} = 0.05$. Filtered signals from the three spanwise stations highlight the dominant role of streamwise oscillations. The peak r.m.s. value of the filtered spanwise-averaged signals accounts for 65 % of the peak r.m.s. value in the full spanwise-direction-filtered signals. The contours of pressure fluctuations superimposed with the iso-lines of $C_f = 0$ at different time

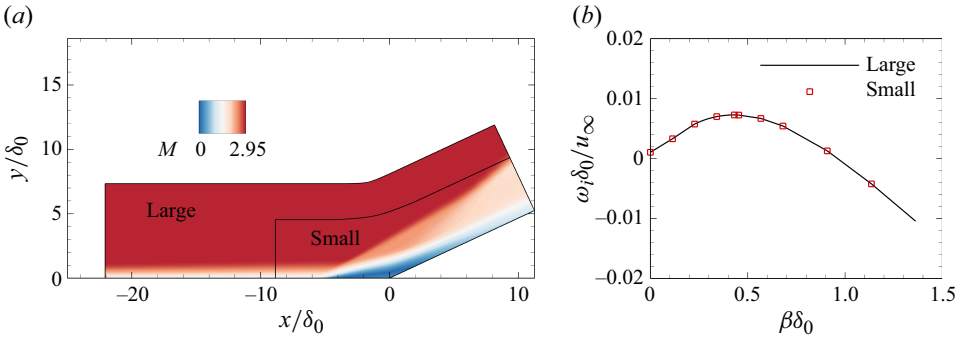

Figure 22. (*a*) Schematic of two computational domains in GSA and (*b*) growth rates as a function of $\beta\delta_0$.

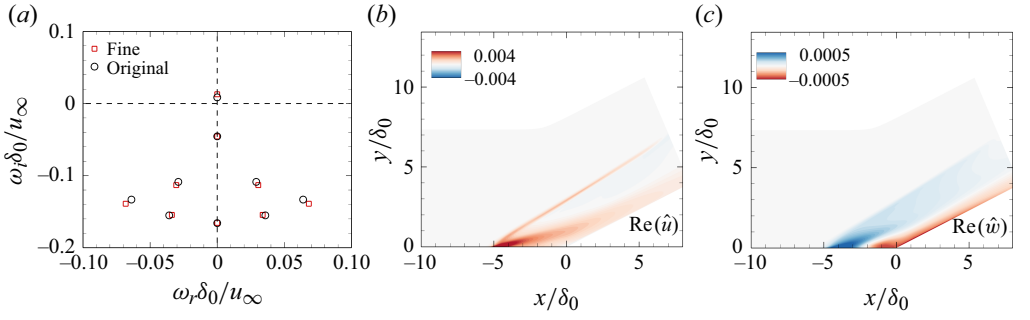

Figure 23. (*a*) Comparison of eigenvalues at $\beta\delta_0 = 0.43$ of two grids. Real parts of (*b*) $\hat{u}$ and (*c*) $\hat{w}$ at $\beta\delta_0 = 0.43$ from the fine grid.

instants reveal the TSB simultaneously undergoing streamwise oscillations and spanwise undulations. Overall, the present study provides new insights into 3-D effects of TSBs in nominally 2-D STBLIs.

However, our study focuses solely on one single case and cannot indicate the generality of the captured structures. Hence, the 65 % dominance ratio only holds in the current case and may vary in other cases under different parameters or interaction types. Future studies will quantify the contributions of these two types of motions to the overall TSBs' dynamics in different cases.

Supplementary movie. Supplementary movie is available at https://doi.org/10.1017/jfm.2025.10496.

Acknowledgements. This work is supported by the National Natural Science Foundation of China (no. 12472239) and the Hong Kong Research Grants Council (no. 15204322).

Declaration of interests. The authors report no conflict of interest.

Appendix A. Verification of GSA

Figure 22 examines the effects of domain size on GSA mode growth rates. A relatively small domain serves as the new base flow for GSA, as illustrated in figure 22(*a*). The growth rates overlap between both domains and share a common peak at $\beta\delta_0 = 0.43$. These results confirm that the current domain size is sufficiently large for stability analysis.

The influence of grid resolution on GSA is then investigated. Results from the original grid (1321×136) and the fine grid (1821×173) share a common peak at $\beta\delta_0 = 0.43$. Figure 23(*a*) compares the eigenvalues of the two meshes at $\beta\delta_0 = 0.43$. The eigenvalues

from the fine mesh are slightly larger than those from the original mesh. Nonetheless, the obtained eigenfunctions shown in figure 23(b–c) exhibit the same features as those in figure 15 at $\beta\delta_0 = 0.43$. These similarities demonstrate that both meshes effectively capture the key dynamical features of the TSB.

References

Abe, H., Mizobuchi, Y., Matsuo, Y. & Spalart, P.R. 2012 Dns and modeling of a turbulent boundary layer with separation and reattachment over a range of reynolds numbers. *Annual Research Briefs* **143**, 311–322.

Abreu, L.I., Cavalieri, A.V.G., Schlatter, P., Vinuesa, R. & Henningson, D.S. 2020 Spectral proper orthogonal decomposition and resolvent analysis of near-wall coherent structures in turbulent pipe flows. *J. Fluid Mech.* **900**, A11.

Beresh, S.J., Clemens, N.T. & Dolling, D.S. 2002 Relationship between upstream turbulent boundary-layer velocity fluctuations and separation shock unsteadiness. *AIAA J.* **40** (12), 2412–2422.

Bernardini, M. & Pirozzoli, S. 2011 Wall pressure fluctuations beneath supersonic turbulent boundary layers. *Phys. Fluids* **23** (8), 085102.

Borgmann, D., Cura, C., Weiss, J. & Little, J. 2024 Three-dimensional nature of low-frequency unsteadiness in a turbulent separation bubble. *AIAA J.* **62** (11), 4349–4363.

Borisov, A.V., Vorontsov, S.S., Zheltovodov, A.A., Pavlov, A.A. & Shpak, S.I. 1993 Development of experimental and computational methods of studies of supersonic separated flows. *Preprint 9–93 ITAM, RAS SB*, Novosibirsk (in Russian).

Borisov, A.V., Zheltovodov, A.A., Maksimov, A.I., Fedorova, N.N. & Shpak, S.I. 1999 Experimental and numerical study of supersonic turbulent separated flows in the neighborhood of two-dimensional obstacles. *Fluid Dyn.* **34** (2), 181–189.

Carini, M., Airiau, C., Debien, A., Léon, O. & Pralits, J.O. 2017 Global stability and control of the confined turbulent flow past a thick flat plate. *Phys. Fluids* **29** (2), 024102.

Ceci, A., Palumbo, A., Larsson, J. & Pirozzoli, S. 2022 Numerical tripping of high-speed turbulent boundary layers. *Theor. Comput. Fluid Dyn.* **36** (6), 865–886.

Ceci, A., Palumbo, A., Larsson, J. & Pirozzoli, S. 2023 On low-frequency unsteadiness in swept shock wave–boundary layer interactions. *J. Fluid Mech.* **956**, R1.

Ceci, A., Palumbo, A., Larsson, J. & Pirozzoli, S. 2024 Low-frequency unsteadiness in hypersonic swept shock wave-boundary layer interactions. *Phys. Rev. Fluids* **9** (5), 054603.

Choi, H. & Moin, P. 2012 Grid-point requirements for large eddy simulation: Chapman's estimates revisited. *Phys. Fluids* **24** (1), 011702.

Chu, B.-T. 1965 On the energy transfer to small disturbances in fluid flow (Part I). *Acta Mechanica* **1** (3), 215–234.

Clemens, N.T. & Narayanaswamy, V. 2014 Low-frequency unsteadiness of shock wave/turbulent boundary layer interactions. *Annu. Rev. Fluid Mech.* **46**, 469–492.

Coleman, G.N., Rumsey, C.L. & Spalart, P.R. 2018 Numerical study of turbulent separation bubbles with varying pressure gradient and reynolds number. *J. Fluid Mech.* **847**, 28–70.

Cura, C., Hanifi, A., Cavalieri, A.V.G. & Weiss, J. 2024 On the low-frequency dynamics of turbulent separation bubbles. *J. Fluid Mech.* **991**, A11.

Dau, K., Borgmann, D., Little, J.C. & Weiss, J. 2023 Investigation of low frequency unsteadiness in the turbulent separation bubble produced by a wall mounted hump. In *AIAA AVIATION. 2023 Forum*, pp. 4008. AIAA.

Dussauge, J.-P., Dupont, P. & Debiève, J.-F. 2006 Unsteadiness in shock wave boundary layer interactions with separation. *Aerosp. Sci. Technol.* **10** (2), 85–91.

Fan, J., Uy, K.C.K., Hao, J. & Wen, C.-Y. 2024 Coexistence of different mechanisms underlying the dynamics of supersonic turbulent flow over a compression ramp. *Phys. Fluids* **36** (1), 016115.

Floryan, J.M. 1991 On the Görtler instability of boundary layers. *Prog. Aerosp. Sci.* **28** (3), 235–271.

Ganapathisubramani, B., Clemens, N.T. & Dolling, D.S. 2007 Effects of upstream boundary layer on the unsteadiness of shock-induced separation. *J. Fluid Mech.* **585**, 369–394.

Ganapathisubramani, B., Clemens, N.T. & Dolling, D.S. 2009 Low-frequency dynamics of shock-induced separation in a compression ramp interaction. *J. Fluid Mech.* **636**, 397–425.

Grilli, M., Hickel, S. & Adams, N.A. 2013 Large-eddy simulation of a supersonic turbulent boundary layer over a compression–expansion ramp. *Intl J. Heat Fluid Flow* **42**, 79–93.

Grilli, M., Schmid, P.J., Hickel, S. & Adams, N.A. 2012 Analysis of unsteady behaviour in shockwave turbulent boundary layer interaction. *J. Fluid Mech.* **700**, 16–28.

HAO, J. 2023 On the low-frequency unsteadiness in shock wave–turbulent boundary layer interactions. *J. Fluid Mech.* **971**, A28.
HAO, J., CAO, S., WEN, C.-Y. & OLIVIER, H. 2021 Occurrence of global instability in hypersonic compression corner flow. *J. Fluid Mech.* **919**, A4.
HAO, J. & WEN, C.-Y. 2020 Hypersonic flow over spherically blunted double cones. *J. Fluid Mech.* **896**, A26.
HAO, J., WEN, C.-Y. & WANG, J. 2019 Numerical investigation of hypervelocity shock-wave/boundary-layer interactions over a double-wedge configuration. *Intl J. Heat Mass Transfer* **138**, 277–292.
HELM, C.M. & MARTÍN, M.P. 2021 Scaling of hypersonic shock/turbulent boundary layer interactions. *Phys. Rev. Fluids* **6** (7), 074607.
HENDRICKSON, T.R., KARTHA, A. & CANDLER, G.V. 2018 An improved ducros sensor for the simulation of compressible flows with shocks. In *2018 Fluid Dynamics Conference*, pp. 3710. AIAA.
HOU, Y.X., CLEMENS, N.J. & DOLLING, D. 2003 Multi-camera piv study of shock-induced turbulent boundary layer separation. In *41st Aerospace Sciences Meeting and Exhibit*, pp. 441. AIAA.
JAMESON, A., SCHMIDT, W. & TURKEL, E. 1981 Numerical solution of the euler equations by finite volume methods using Runge–Kutta time stepping schemes. In *14th Fluid and Plasma Dynamics Conference*, pp. 1259. AIAA.
JENQUIN, C., JOHNSON, E.C. & NARAYANASWAMY, V. 2023 Investigations of shock–boundary layer interaction dynamics using high-bandwidth pressure field imaging. *J. Fluid Mech.* **961** , A5.
JIANG, G.-S. & SHU, C.-W. 1996 Efficient implementation of weighted eno schemes. *J. Comput. Phys.* **126** (1), 202–228.
LI, X., ZHANG, Y., YU, H., LIN, Z.-K., TAN, H.-J. & SUN, S. 2022 Görtler vortices behavior and prediction in dual-incident shock-wave/turbulent-boundary-layer interactions. *Phys. Fluids* **34** (10), 106103.
LILLY, D.K. 1992 A proposed modification of the Germano subgrid-scale closure method. *Phys. Fluids A* **4**, 633–635.
LIOU, M.-S. 2006 A sequel to AUSM, Part II: AUSM+-up for all speeds. *J. Comput. Phys.* **214** (1), 137–170.
LIU, X., CHEN, L., ZHANG, Y., TAN, H., LIU, Y. & PENG, D. 2024 Spanwise unsteadiness in the sidewall-confined shock-wave/boundary-layer interaction. *J. Fluid Mech.* **987**, R6.
LOGINOV, M.S., ADAMS, N.A. & ZHELTOVODOV, A.A. 2006 Large-eddy simulation of shock-wave/turbulent-boundary-layer interaction. *J. Fluid Mech.* **565**, 135–169.
LUHAR, M., SHARMA, A.S. & MCKEON, B.J. 2014 On the structure and origin of pressure fluctuations in wall turbulence: predictions based on the resolvent analysis. *J. Fluid Mech.* **751**, 38–70.
LUMLEY, J.L. 2007 *Stochastic Tools in Turbulence*. Courier Corporation.
MANI, A. 2012 Analysis and optimization of numerical sponge layers as a nonreflective boundary treatment. *J. Comput. Phys.* **231** (2), 704–716.
MCKEON, B.J. & SHARMA, A.S. 2010 A critical-layer framework for turbulent pipe flow. *J. Fluid Mech.* **658**, 336–382.
NICHOLS, J.W., LARSSON, J., BERNARDINI, M. & PIROZZOLI, S. 2017 Stability and modal analysis of shock/boundary layer interactions. *Theor. Comput. Fluid Dyn.* **31**, 33–50.
PASQUARIELLO, V., HICKEL, S. & ADAMS, N.A. 2017 Unsteady effects of strong shock-wave/boundary-layer interaction at high Reynolds number. *J. Fluid Mech.* **823**, 617–657.
PIPONNIAU, S., DUSSAUGE, J.-P., DEBIEVE, J.-F. & DUPONT, P. 2009 A simple model for low-frequency unsteadiness in shock-induced separation. *J. Fluid Mech.* **629**, 87–108.
PIROZZOLI, S. 2010 Generalized conservative approximations of split convective derivative operators. *J. Comput. Phys.* **229** (19), 7180–7190.
PIROZZOLI, S. & GRASSO, F. 2006 Direct numerical simulation of impinging shock wave/turbulent boundary layer interaction at M = 2.25. *Phys. Fluids* **18** (6), 065113.
PIROZZOLI, S., LARSSON, J., NICHOLS, J.W., BERNARDINI, M., MORGAN, B.E. & LELE, S.K. 2010 Analysis of unsteady effects in shock/boundary layer interactions. In *Proceedings of the Summer Program*, pp. 153–164. Center of Turbulence Research.
PLOTKIN, K.J. 1975 Shock wave oscillation driven by turbulent boundary-layer fluctuations. *AIAA J.* **13** (8), 1036–1040.
PRIEBE, S. & MARTÍN, M.P. 2012 Low-frequency unsteadiness in shock wave–turbulent boundary layer interaction. *J. Fluid Mech.* **699**, 1–49.
PRIEBE, S., TU, J.H., ROWLEY, C.W. & MARTÍN, M.P. 2016 Low-frequency dynamics in a shock-induced separated flow. *J. Fluid Mech.* **807**, 441–477.
RAIESI, H., PIOMELLI, U. & POLLARD, A. 2011 Evaluation of turbulence models using direct numerical and large-eddy simulation data. *J. Fluids Engng* **133** (2), 021203.
REAU, N. & TUMIN, A. 2002 On harmonic perturbations in a turbulent mixing layer. *Eur. J. Mech. - B/Fluids* **21** (2), 143–155.

REYNOLDS, W.C. & HUSSAIN, A.K.M.F. 1972 The mechanics of an organized wave in turbulent shear flow. Part 3. Theoretical models and comparisons with experiments. *J. Fluid Mech.* **54** (2), 263–288.

ROSSITER, J.E. 1964 Wind tunnel experiments on the flow over rectangular cavities at subsonic and transonic speeds. *Tech. Rep.* 3438. Aeronautical Research Council Reports and Memoranda.

SCHMIDT, O.T., TOWNE, A., RIGAS, G., COLONIUS, T. & BRÈS, G.A. 2018 Spectral analysis of jet turbulence. *J. Fluid Mech.* **855**, 953–982.

SCHUELEIN, E. & TROFIMOV, V.M. 2011 Steady longitudinal vortices in supersonic turbulent separated flows. *J. Fluid Mech.* **672**, 451–476.

SORENSEN, D., LEHOUCQ, R., YANG, C. & MASCHHOFF, K. 1996 Arpack software, version 2.3.

SOUVEREIN, L.J., DUPONT, P., DEBIEVE, J.-F., DUSSAUGE, J.-P., VAN, O., BAS, W. & SCARANO, F. 2010 Effect of interaction strength on unsteadiness in shock-wave-induced separations. *AIAA J.* **48** (7), 1480–1493.

TONG, F., YU, C., TANG, Z. & LI, X. 2017 Numerical studies of shock wave interactions with a supersonic turbulent boundary layer in compression corner: turning angle effects. *Comput. Fluids* **149**, 56–69.

TOUBER, E. & SANDHAM, N.D. 2009 Large-eddy simulation of low-frequency unsteadiness in a turbulent shock-induced separation bubble. *Theor. Comput. Fluid Dyn.* **23**, 79–107.

TOUBER, E. & SANDHAM, N.D. 2011 Low-order stochastic modelling of low-frequency motions in reflected shock-wave/boundary-layer interactions. *J. Fluid Mech.* **671**, 417–465.

TOWNE, A., SCHMIDT, O.T. & COLONIUS, T. 2018 Spectral proper orthogonal decomposition and its relationship to dynamic mode decomposition and resolvent analysis. *J. Fluid Mech.* **847**, 821–867.

VAN, D. & EDWARD, R. 1951 Turbulent boundary layer in compressible fluids. *J. Aeronaut. Sci.* **18** (3), 145–160.

WELCH, P. 1967 The use of fast Fourier transform for the estimation of power spectra: a method based on time averaging over short, modified periodograms. *IEEE Trans. Audio Electroacoust.* **15** (2), 70–73.

WU, X. & MOIN, P. 2009, Direct numerical simulation of turbulence in a nominally zero-pressure-gradient flat-plate boundary layer. *J. Fluid Mech.* **630**, 5–41.

ZHANG, Z., HAO, J. & UY, K.C.K. 2025 Characterising görtler vortices in supersonic turbulent flows over concave surfaces. *J. Fluid Mech.* **1012**, A29.

ZHELTOVODOV, A.A., TROFIMOV, V.M., SCHUELEIN, E. & YAKOVLEV, V.N. 1990 An experimental documentation of supersonic turbulent flows in the vicinity of sloping forward-and backward-facing ramps, *Rep No 2030*. Institute of Theoretical.

ZHUANG, Y., TAN, H.-J., LIU, Y.-Z., ZHANG, Y.-C. & LING, Y. 2017 High resolution visualization of Görtler-like vortices in supersonic compression ramp flow. *J. Vis.* **20**, 505–508.